Onset of Maikop sedimentation and cessation of Eocene arc volcanism in the Talysh Mountains, Azerbaijan

A. VAN DER BOON[1]*, K. F. KUIPER[2], G. VILLA[3], W. RENEMA[4], M. J. M. MEIJERS[5,6], C. G. LANGEREIS[1], E. ALIYEVA[7] & W. KRIJGSMAN[1]

[1]*Paleomagnetic Laboratory Fort Hoofddijk, Utrecht University, Budapestlaan 17, 3584 CD Utrecht, the Netherlands*

[2]*Vrije Universiteit Amsterdam, De Boelelaan 1085, 1081 HV, Amsterdam, the Netherlands*

[3]*Department of Physics and Earth Sciences, Università degli studi di Parma, Parma, Italy*

[4]*Naturalis Biodiversity Center, Darwinweg 2, 2333 CR, Leiden, the Netherlands*

[5]*Université de Nice – Sophia Antipolis, UMR Géoazur, Observatoire de la Côte d'Azur, 250 rue Albert Einstein, 06560 Valbonne, France*

[6]*Department of Earth Sciences, University of Minnesota, 291 Shepherd Laboratories, 100 Union Street SE, Minneapolis, MN 55455, USA*

[7]*Institute of Geology ANAS, H. Javid av., 29A, Baku, 1143, Azerbaijan*

*Correspondence: a.vanderboon@uu.nl

Abstract: The Maikop Series forms an important source rock in the former Paratethys. Deposition is often interpreted as anoxic, linked to restriction of the Paratethys. The Pirembel formation in the Talysh Mountains (Azerbaijan) is attributed to the Maikop Series and was deposited above the Eocene volcanic Peshtasar formation. Dating the onset of anoxia could help to distinguish glacio-eustatic from tectonic causes of restriction. We integrated magnetostratigraphy and biostratigraphy to date the onset of Pirembel sedimentation and used geochemistry to characterize the tectonic setting of the Peshtasar volcanic rocks. The onset of Maikop sedimentation in the Talysh was determined to be 37.7 Ma, ruling out a link with the major sea-level drop at the Eocene–Oligocene Transition (33.9 Ma) and favouring a tectonic cause. Extrapolating the average sedimentation rate (34 cm kyr) suggests that the entire Pirembel formation belongs to the Late Eocene. We hypothesize that the end of volcanism is important in the transition to Pirembel sedimentation. The palaeomagnetic and geochemistry results for the volcanic rocks cluster in three groups, suggesting three distinct episodes of volcanism. Volcanic sills within the Eocene Arkevan formation plot exactly on these groups, confirming the relationship between the Arkevan and Peshtasar formations. Volcanic rocks of the Talysh show continental-arc signatures and may be related to an Eocene volcanic belt extending towards southeastern Iran.

Supplementary material: The full analytical data of the Ar–Ar dating are available at http://www.geolsoc.org.uk/SUP18851

The Maikop Series was deposited in the Paratethys, an epicontinental sea extending from Germany to China during the Palaeogene (Fig. 1a). The Maikop Series predominantly consists of black shales that are the most important source rock for hydrocarbons in the South Caspian Basin and are thus of great economic importance. Black shales generally contain a relatively large amount of unoxidized carbon and are usually deposited under anoxic, reducing conditions (Passier *et al.* 1999; Efendiyeva 2004; Hudson *et al.* 2008; Sachsenhofer *et al.* 2009; Johnson *et al.* 2010). Oxygen levels were lowest during the deposition of the lower part of the Maikop Series (Hudson *et al.* 2008), but generally ranged from anoxic to suboxic (0.0–0.2 ml/l O_2; Hudson *et al.* 2008). Anoxia is associated with stagnant water columns, which are generally related to decreased basin circulation (Tyson & Pearson 1991; Soták 2010). The onset of Maikop sedimentation thus marks a major change in the palaeoenvironmental conditions in the Paratethys basin, which is most likely to be related to the restriction of water circulation between the Paratethys and the open ocean (Steininger & Wessely 2000; Schulz *et al.* 2005; Hudson *et al.* 2008; Jovane *et al.* 2009; Johnson *et al.* 2010).

(a)

(b)
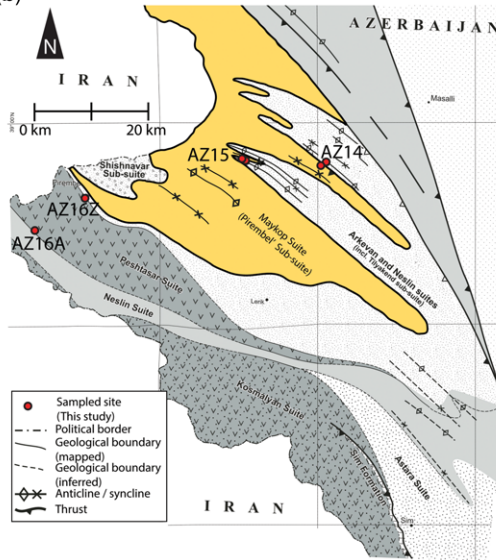
After: Vincent et al., 2005

(c)

After: Alizadeh et al., 2005

Fig. 1. (**a**) Early Oligocene (Pshekhian) palaeogeographic reconstruction of Rögl (1998) drawn on the present political boundaries of Europe. Dark blue represents the outer limits of the Pa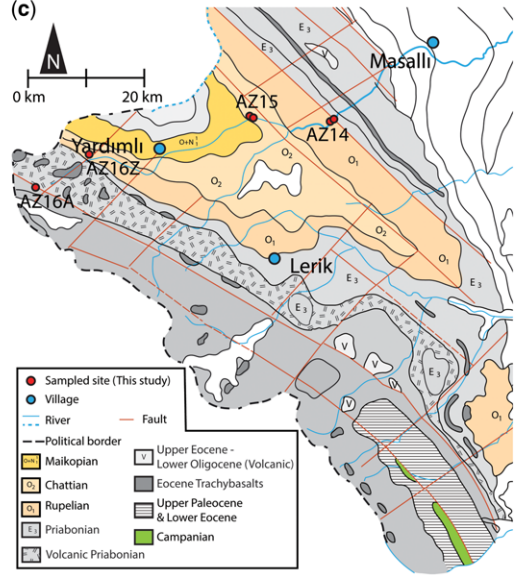ratethys from the reconstruction of Popov *et al.* (2004). Cross-hatch represents the present-day distribution of Oligocene Paratethys sediments according to Veto (1987). Red rectangle represents the location of the study area. (**b**) Location of sampled sections of this study and distribution of Maikop sediments on the geological map modified from Vincent *et al.* (2005). (**c**) Location of sampled sections of this study and distribution of Oligocene and Maikop sediments on the geological map modified after Alizadeh *et al.* (2005).

The prevailing hypothesis for the Maikop Series places the onset of anoxia in the Late Eocene to Early Oligocene, with anoxic conditions continuing into the Early Miocene (Abrams & Narimanov 1997; Hudson *et al.* 2008; Popov *et al.* 2008).

There are two main processes that can explain a restriction event in this time interval: (1) tectonic uplift related to plate convergence between Arabia and Eurasia, leading to the disconnection of the marine gateways; and (2) a major sea-level drop

at the Eocene–Oligocene Transition (EOT) at 33.9 Ma (e.g. Steininger & Wessely 2000; Zachos *et al.* 2001; Schulz *et al.* 2005; Jovane *et al.* 2009).

Precise dating of the Maikop Series could potentially distinguish between these geodynamic and climatic processes. If the onset of anoxia exactly coincides with the EOT, glacio-eustatic sea-level lowering is a very likely cause. Anoxia might have, in turn, increased carbon burial, leading to further global cooling. If, however, the onset of anoxia had already started during the Eocene, the tectonic collision of Africa and Arabia with Eurasia may be a more likely cause for the restriction of water exchange. The timing of this collision is still poorly constrained, but it probably took place between 39 and 20 Ma (Ballato *et al.* 2011; McQuarrie & van Hinsbergen 2013). If collision occurred around the EOT, the respective roles of climate and tectonics will be difficult to distinguish.

This research aimed to date the onset of Maikop deposition in the Talysh Mountains of Azerbaijan (Figs 1b, c & 2) to resolve the mechanism that initiated the anoxic conditions in this part of the Parathethys basin.

A thick succession of volcanic rocks is present underneath the Maikop sediments in the Talysh, linked to the Alborz Magmatic Arc (AMA) in the east (Vincent *et al.* 2005; Asiabanha & Foden 2012) and to the Adjara–Trialet zone of Turkey and Georgia in the west (Golonka 2004; Brunet *et al.* 2003; Asiabanha & Foden 2012). Much controversy exists about the tectonic setting of these volcanic belts (e.g. Yilmaz *et al.* 2000). Two contrasting settings are proposed: an arc setting and a back-arc setting.

A multidisciplinary stratigraphic approach based on magnetostratigraphy, biostratigraphy and X-ray fluorescence (XRF) analyses has been used to obtain constraints on the timing of the onset of anoxia and the tectonic setting in which the volcanic rocks were deposited. Furthermore, samples of various lithologies (sandstones, siltstones and shales) were taken for biostratigraphic analyses. Ar–Ar dating was performed on basalts from the two formations that contained volcanic rocks.

Geological background

The Talysh Mountains are situated in the southernmost part of Azerbaijan (Figs 1a & 2), bordering the Caspian Sea and Iran. The Talysh Mountains are located within the active collision zone between Arabia and Eurasia and continue into the Iranian
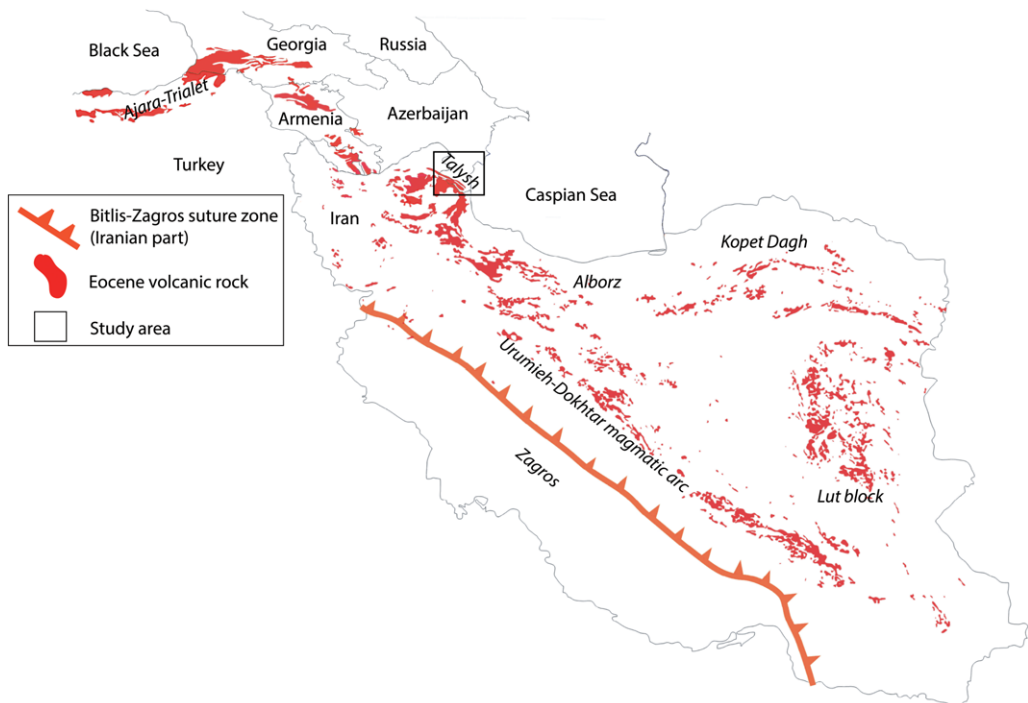

Fig. 2. Regional map showing the distribution of Eocene volcanic rocks (after maps of Nalivkin 1976; Allen & Armstrong 2008; Agard *et al.* 2011) and the names of relevant areas.

Talesh, which form the western part of the Alborz mountain belt. The Alborz Mountains pass into the Kopet Dagh in the east. The lithology of the Talysh is composed of a succession of predominantly Eocene–Oligocene volcanic rocks and sediments. The volcanic rocks are mainly high-K alkali basalts, which, according to Asiabanha & Foden (2012), Golonka (2004) and Vincent *et al.* (2005), formed in a back-arc system. Their geochemical signatures (Nb troughs, Th spikes, large ion lithophile element (LILE) and Sr enrichment, and relative heavy rare earth element depletion), however, are characteristic of magmatic arcs (Vincent *et al.* 2005; Verdel *et al.* 2011; Asiabanha & Foden 2012).

To the SE of the Talysh (in Iran), another magmatic belt of Eocene age has been reported. This is the Urumieh–Dokhtar Magmatic Arc (UDMA), which runs from Urmia in the NW of Iran to Bazman in the SE (Fig. 2). This belt consists of subduction-related magmas (e.g. Ghorbani 2006; Verdel *et al.* 2011). The subduction of the Arabian plate underneath the Eurasian plate took place along the Zagros–Bitlis suture zone (Agard *et al.* 2011; Asiabanha & Foden 2012; Mouthereau *et al.* 2012).

In the Talysh, the Paleocene and Eocene rocks mostly consist of volcanic rocks and volcanogenic sediments, but a consensus on their age is still lacking (Alizadeh *et al.* 2005; Vincent *et al.* 2005) (Fig. 1b, c). According to Alizadeh *et al.* (2005), the lowermost Palaeogene unit is the Astara formation of Paleocene age. It consists of tuffaceous sandstones, siltstones and mudstones, which are unconformably overlain by the volcanic rocks of the Kosmalyan formation (Lower Eocene). However, Vincent *et al.* (2005) infer that the Astara formation is a lateral equivalent of the Kosmalyan formation. ^{40}Ar–^{39}Ar dating on samples from a sill intruded into the Astara formation constrains its lower part as older than 40.7 Ma (Vincent *et al.* 2005).

The volcanic rocks of the Kosmalyan formation are overlain by sedimentary rocks (sandstones, siltstones and shales) of the Neslin formation and a second volcanic unit; the Peshtasar formation (Fig. 3). The volcanic Peshtasar rocks are considered to be partly equivalent to the sandstone-dominated Arkevan formation. The thickness of the Arkevan formation varies considerably, showing a thickening trend towards the east (Vincent *et al.* 2005). The transition from the sandstone-dominated Arkevan formation to the mudstone-dominated Pirembel formation of the Maikop Series is marked by the sudden disappearance of metre-thick sandstone beds (Fig. 4). The Pirembel formation contains many dark grey to black very fine silt layers. Shales in the classical sense (that have a mud grain size) are scarce. The study of Vincent *et al.* (2005) presents a more detailed (sedimentological) description of the formations in the Talysh Mountains.

Sections and lithology

Several long and continuous outcrops of the Maikop Series are exposed in the Talysh Mountains of Azerbaijan. We sampled three sections and follow the nomenclature of Vincent *et al.* (2005). The locations of all sampled sections are plotted on the geological maps of Vincent *et al.* (2005) and Alizadeh *et al.* (2005) (Fig. 1b, c). This shows that section AZ15 represents the onset of Maikop sediments in both stratigraphic concepts. Section AZ16 covers the entire volcanic Peshtasar formation, with the lowest sampled flow, AZ16A, just above the sediments of the Neslin formation (Fig. 3).

AZ14 is located near Tilyakend (38.948605°N, 48.509431°E) and consists of sandstones, siltstones and basalts. The section consists of several volcanic sills intercalated in the sands of the Eocene Arkevan formation (Vincent *et al.* 2005). The same section is considered by Alizadeh *et al.* (2005) to be of Oligocene age (Fig. 1b, c).

Section AZ15 (38.953597°N, 48.381920°E) is a sedimentary succession with sandstones, siltstones and shales (Fig. 4). The Arkevan–Pirembel transition is marked by a change in lithology at 118 m in our sampled section. Above this level, hardly any thick sand layers are present, whereas they are abundant below. Sands that are 1 m thick or more are horizontally exaggerated in Figure 4 to show that the thick sand beds decrease in thickness and abundance higher up in the stratigraphy.

Section AZ16 (for GPS coordinates, see Fig. 5) consists mostly of Peshtasar basalts, with very few sedimentary beds in between. No lithostratigraphic log has been made because the different volcanic units are hard to distinguish in the field. The section is made up of basalts (pillow basalts according to Vincent *et al.* 2005) with some interbedded sediments (allowing correction for bedding tilt). Blocks of sediments and sedimentary intercalations within the section were observed between sites AZ16F, AZ16G and AZ16H (see also Fig. 3) and between AZ16K and AZ16L, possibly indicating periods of magmatic quiescence.

Materials and methods

Over 500 standard palaeomagnetic samples (25 mm diameter cores) were drilled using a gasoline-powered drill and an electrical drill. The cores were cut in the laboratory into standard (22 mm) specimens. Basalt samples with a high natural remanent magnetization were subsequently cut in half.

Palaeomagnetism

The magnetic susceptibility at room temperature of every second sample of AZ15 was measured using
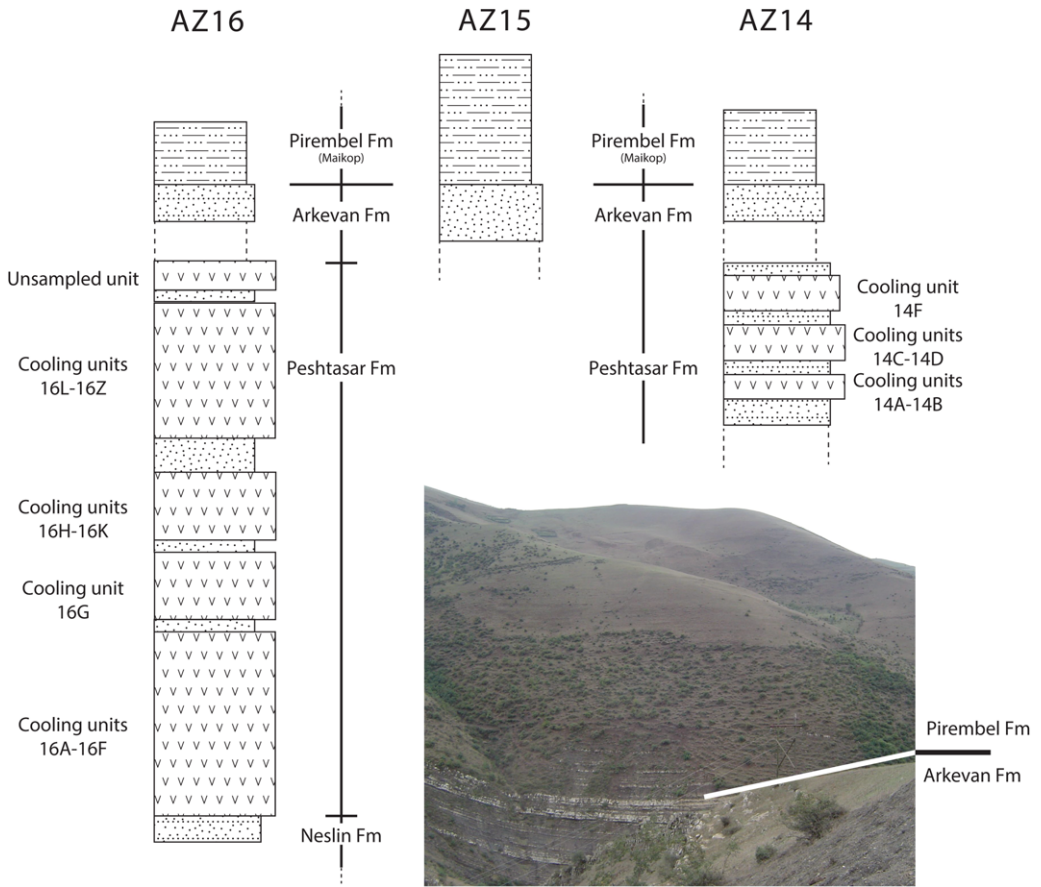
Fig. 3. Schematic logs of the three sampled sections of this study and photograph of two marker beds in the top of the Arkevan formation.

an AGICO KLY-3 Kappa bridge. Measured values for the susceptibility were mass-normalized. Changes in magnetic susceptibility throughout a section may reflect variations in the lithology caused, for example, by variations in detrital input (Hay 1996, 1998; Ellwood *et al.* 2000) or variations in climate and environment resulting in changing diagenetic conditions (e.g. Da Silva *et al.* 2012).

To assess the magnetic carriers of the samples as well as chemical alteration temperatures, thermomagnetic analyses were carried out in air using a modified horizontal translation Curie balance (Mullender *et al.* 1993). The magnetization of powdered samples was measured as a function of temperature during six cycles up to increasingly elevated temperatures ($700°C$ maximum; heating and cooling rate $10°C/min$). The magnetic susceptibility of the samples was measured as a function of temperature on an AGICO KLY-3S susceptometer with a CS-3 furnace attachment (measurement frequency

976 Hz, field strength 400 A m^{-1} peak level, noise level 2×10^{-7} SI). Measurements were performed on crushed basalt samples; again, six heating and cooling cycles were performed on powdered samples up to a temperature of $600°C$.

A total of 107 samples were cored at section AZ14: at least seven samples per level were taken from five cooling units and sediments between the cooling units were also sampled. A total of 221 samples from sediments were analysed at section AZ15. A total of 26 levels were sampled in volcanic section AZ16, with at least seven samples per level. Each level was sampled in a different magmatic cooling unit. The specimens were subjected to thermal and/or alternating field (AF) demagnetization. Temperature increments of $20–60°C$ were applied to thermally demagnetize the samples in a shielded ASC oven up to a maximum temperature of $580°C$ for basalts and approximately $400°C$ for sediments to avoid thermal alteration as a result of the presence
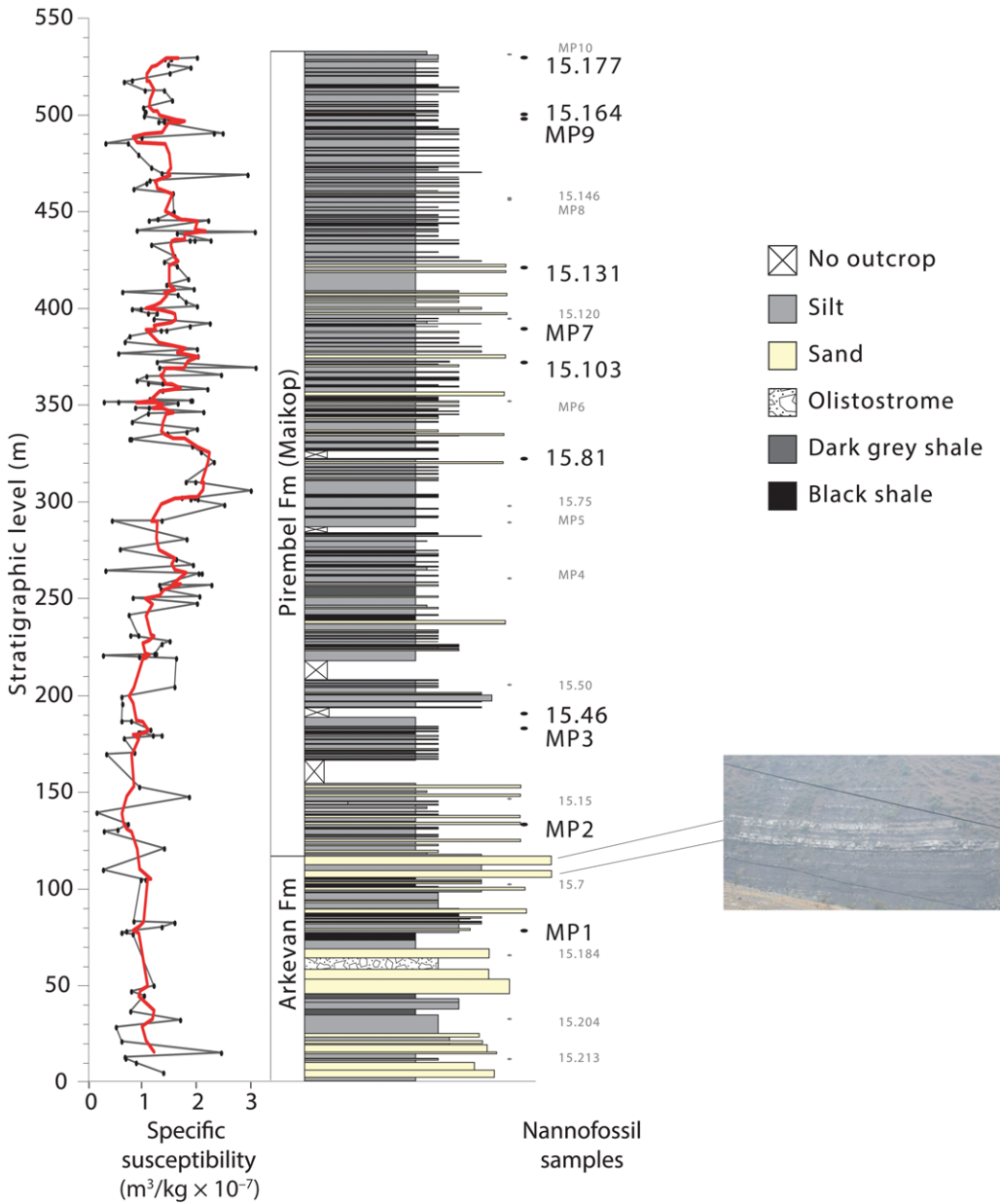
Fig. 4. Lithostratigraphic log of section AZ15 with susceptibility results. Thick red line represents weighted average over five samples.

of pyrite. Several samples were stepwise AF demagnetized after thermal demagnetization at 150, 175 or 200°C to remove the high coercivity components resulting from possible low temperature oxidation (weathering) (Van Velzen & Zijderveld 1995). Demagnetization steps of 5–100 mT were applied. Another part of the samples was demagnetized using three or five steps (20, 100, 150 and, sometimes, 175 and 200°C) of thermal demagnetization prior to AF demagnetization. The magnetization after each step was measured on a 2G Enterprise horizontal cryogenic magnetometer equipped with three DC SQUIDS (noise level 3×10^{-12} Am^2) with a robotized 2G DC-SQUID magnetometer

Unit	N	k	a95	dec	inc	tectonic correction strike	dip	dec tc	inc tc	GPS coordinates N	E	Ar-Ar sample
16A	8	66.1	6.9	206.0	-19.5	291	17	206.2	-2.1	38.86672	48.05018	See text for discussion
16B	7	125.0	5.4	227.1	-11.3	291	17	226.2	4.0	38.87484	48.06173	
16C	7	10.9	19.2	225.6	-9.0	291	17	225.4	6.5	38.87750	48.06395	
16D	9	116.8	4.8	207.5	-25.4	291	17	207.0	-8.5	38.87975	48.07098	No reliable age
16E	7	46.7	8.9	205.9	-39.4	291	17	205.1	-22.4	38.88131	48.07336	
16F	8	64.8	6.9	208.4	-7.9	291	17	208.4	9.0	38.88290	48.07519	
16G	8	5.6	25.7	205.6	-28.5	291	17	205.1	-11.6	38.88549	48.07825	
16H	7	69.5	7.3	209.8	-27.9	291	17	208.9	-11.1	38.88925	48.08513	
16I	7	68.6	7.3	218.3	-4.9	291	17	204.0	-1.9	38.89417	48.09118	
16J	7	42.8	9.3	224.4	-25.8	291	17	222.3	-10.0	38.89596	48.09346	
16K	7	55.5	8.2	200.0	-26.5	291	17	199.7	-9.2	38.89577	48.09434	
16L	7	109.6	5.8	209.6	-77.1	293	12	206.5	-65.1	38.90005	48.09632	
16M	9	76.2	5.9	235.2	-76.0	293	12	220.8	-65.0	38.90105	48.09660	
16N	7	80.2	6.8	242.5	-62.5	293	12	233.9	-53.2	38.90586	48.10180	No reliable age
16O	7	80.5	6.8	205.1	-73.1	293	12	205.0	-60.1	38.90645	48.10301	
16P	6	65.6	8.3	231.7	-66.3	293	12	222.9	-55.3	38.90757	48.10542	
16Q	7	52.5	8.4	133.6	-25.8	295	21	141.4	-17.7	38.91190	48.10588	
16R	7	84.8	6.6	129.8	-22.1	295	21	136.7	-15.5	38.91399	48.10417	
16S	7	12.0	18.2	155.0	-7.9	295	21	155.3	5.8	38.91090	48.10873	No reliable age
16T	7	132.0	5.3	235.9	-58.7	293	12	228.0	-48.2	38.90729	48.11422	
16U	7	54.3	8.3	225.6	-65.1	293	12	218.9	-53.8	38.90733	48.11948	
16V	7	12.3	17.9	132.8	-11.8	290	22	135.7	-4.8	38.90757	48.12012	No reliable age
16W	7	17.6	14.8	123.8	-24.1	290	22	128.8	-10.9	38.54530	48.07425	
16X	7	89.4	6.4	127.6	-21.5	290	22	134.4	-15.6	38.54528	48.07487	
16Y	7	60.3	7.8	135.7	-20.1	290	22	141.2	-11.6	38.54519	48.07571	No reliable age
16Z	7	82.9	6.7	138.3	-20.5	290	22	143.7	-11.2	38.54451	48.07971	

			N	dec	inc	k	a95
Average (no cutoff) notc		Group I	11	213.0	-20.8	33.6	8.0
		Group II	7	229.0	-68.8	90.6	6.4
		Group III	8	134.7	-19.5	55.3	7.5
Average (no cutoff) tc		Group I	11	209.0	-7.7	28.4	8.7
		Group II	7	220.2	-57.6	91.0	6.4
		Group III	8	139.7	-10.3	55.9	7.5

Fig. 5. Summary of palaeomagnetic results for section AZ16.

(dynamic range 3×10^{-12} to 5×10^{-5} Am^2). The results were analysed using orthogonal vector diagrams (Zijderveld 1967) and the characteristic remanent magnetization (ChRM) directions were determined using principal components analysis (Kirschvink 1980). The mean directions were determined using standard Fisher statistics and standard errors were calculated following Butler (1992) and the criteria of Deenen *et al.* (2011*b*).

$^{40}Ar–^{39}Ar$ dating

We selected ten cooling units for $^{40}Ar/^{39}Ar$ dating. The samples were processed using standard mineral separation techniques. The samples were first crushed, washed and dried. Heavy liquid separation was performed on size fractions between 250 and 500 µm with densities of 2.75 and 2.81 g/cm^3 to remove the xenocrysts from the groundmass. In a few cases the 125–250 µm fraction was used. All the groundmass separates were finally hand-picked under a microscope. Samples and standards (Fish Canyon tuff sanidine; Kuiper *et al.* 2008) were wrapped in aluminium foil and irradiated for 18 hours in the High Flux Reactor, Petten, the Netherlands in the Cd-shielded RODEO-P3 position. Groundmass samples were loaded into 21-hole trays in 6 mm pits, placed in an ultra-high vacuum system and baked in two steps: for two days at 250°C in a vacuum system at $<10^{-5}$ mbar, followed by a one-day bake-out in the extraction line at *c.* 125°C. The samples were heated stepwise using a Synrad 48–5 CO_2 laser and custom-made beam delivery system. The released gas was purified in a sample clean-up line designed in-house (St172, NP10 and Ti getters) and analysed on an MAP215–50 noble gas mass spectrometer fitted with a Balzers SEV217 detector. Mass discrimination was monitored regularly by three replicate runs of air pipettes at least every 12–24 hours. Blanks were run for every three to four unknowns. Ages were calculated using the in-house developed ArArCalc software (Koppers 2002) relative to the Fish Canyon tuff sanidine of 28.201 ± 0.23 Ma (Kuiper *et al.* 2008) using the decay constants of Min *et al.* (2001) (see discussion in Kuiper *et al.* 2008). The $^{40}Ar/^{36}Ar$ ratio of 298.56 of Lee *et al.* (2006) was used in the calculations. Errors are reported at the 2σ level.

Micropalaeontology

Calcareous nannofossils were analysed from 25 samples of section AZ15. Smear slides were made following standard techniques (Bown & Young 1998). Quantitative analyses were unattainable as a result of the extreme scarcity of the assemblage. To classify most of the species, an optical microscope at 1250× magnification was used with both crossed nicols and phase contrast. Analyses were extended for at least 400 fields of view.

Geochemistry

The chemical compositions of all the cooling units of sections AZ14 and AZ16 were determined at Vrije Universiteit in Amsterdam, the Netherlands, using XRF spectrometry. The samples were crushed using a jaw-crusher, then powdered using several agate mills. The powders were dried overnight in an oven at 110°C. For each sample, a bead was made for major element analysis. The samples were oxidized for 30 minutes in a muffle furnace at a temperature of 1000°C. The samples were weighed before and after heating to calculate the loss on ignition (LOI). After oxidation, approximately 1.0 g of each sample was mixed with four times this amount of lithium metaborate ($LiBO_2$) flux. The samples were subsequently shaken for ten minutes. Beads were created using the Perl'X3 furnace and pellets were created of the dried, unoxidized powder, which was mixed with a binding resin (EMU powder). About 4.5 g of sample were mixed with 10% EMU for 15 minutes. The pellets were pressed at a pressure of 20 tonnes. Beads and pellets were analysed on a Panalytical MagiX Pro (PW2440) instrument using different programmes of XRF. The accuracy and precision of the measurements were based on the measurement of four international standards analysed between 2003 and 2011 (Handley *et al.* 2007) (see http://www.falw.vu/~petrolab/xrf).

Results

Palaeomagnetism

Arkevan formation (AZ14). The palaeomagnetic results for both the sedimentary and volcanic samples of AZ14 are ambiguous. Many of the demagnetization diagrams showed a clustering at the high temperature/high coercivity steps and the magnetization did not decrease towards the origin. For these samples, no reliable directions or polarities could be determined (see Van der Boon 2013).

Arkevan–Pirembel transition (AZ15). The bulk magnetic susceptibility record of section AZ15 does not show any major trend (Fig. 4). The

sampling resolution appears to be insufficient to observe any clear cyclic variations and a much higher resolution than the palaeomagnetic sampling (which was targeted only at the most promising lithologies) seems to be required. On average, the susceptibility is slightly higher in the upper half of the section (see the five-point moving average in Fig. 4). However, a lower resolution leading to a sampling bias in the lower half of the section could account for this effect.

Thermomagnetic runs of three different lithologies were performed (siltstones, grey mudstones and sandstones, Fig. 6n–p). The magnetization decreases gradually on heating and shows reversible behaviour up to *c.* 400°C. The magnetization significantly increases above this temperature and the curves become irreversible. The magnetization increases up to a temperature of 500°C, after which it decreases up to a temperature of 580°C. For the siltstone sample (AZ15.26; Fig. 5n), a very slight decrease can be observed at 680°C, suggesting the presence of some hematite. The decrease in magnetization up to about 350–400°C can be explained by the breakdown of iron sulphides. The increase in magnetization from 400 to 500°C is caused by the oxidation of iron sulphides, most probably pyrite, converting to magnetite between 380 and 420°C. These newly formed magnetic minerals are removed at 580°C, confirming the formation of magnetite.

Representative Zijderveld diagrams of samples of section AZ15 (Fig. 6b–m) show variable demagnetization. Many samples show a random 'spaghetti plot' behaviour, mainly caused by very low intensities that are of the order of the noise level of the magnetometer (Fig. 6g, i), apart from a viscous component that is removed at the very first demagnetization step. For a number of samples it is not certain whether the normal polarity is of primary origin or results from a present-day field overprint (Fig. 6f). In distinguishing the ChRM from a recently acquired normal polarity, we have used the criterion of 'gradual' decay at higher fields or temperatures (probably the ChRM residing in magnetite or an iron sulphide) v. very fast decay at low fields/ temperatures (probably a recent overprint). For samples yielding a reversed polarity, the interpretation is more straightforward, varying from 'probably' reversed (Fig. 6d, e) to clearly reversed (Fig. 6b, c).

In the magnetostratigraphic column (Fig. 6a), we have indicated when we consider that a sample carries a primary magnetization, depending on the described criteria and on the consistency of the magnetostratigraphy. If the results are inconsistent, of low quality and/or probably overprinted, we have not assigned any polarity signature (grey shaded levels in Fig. 6a). Plotting all the results in stratigraphic order reveals at least three polarity
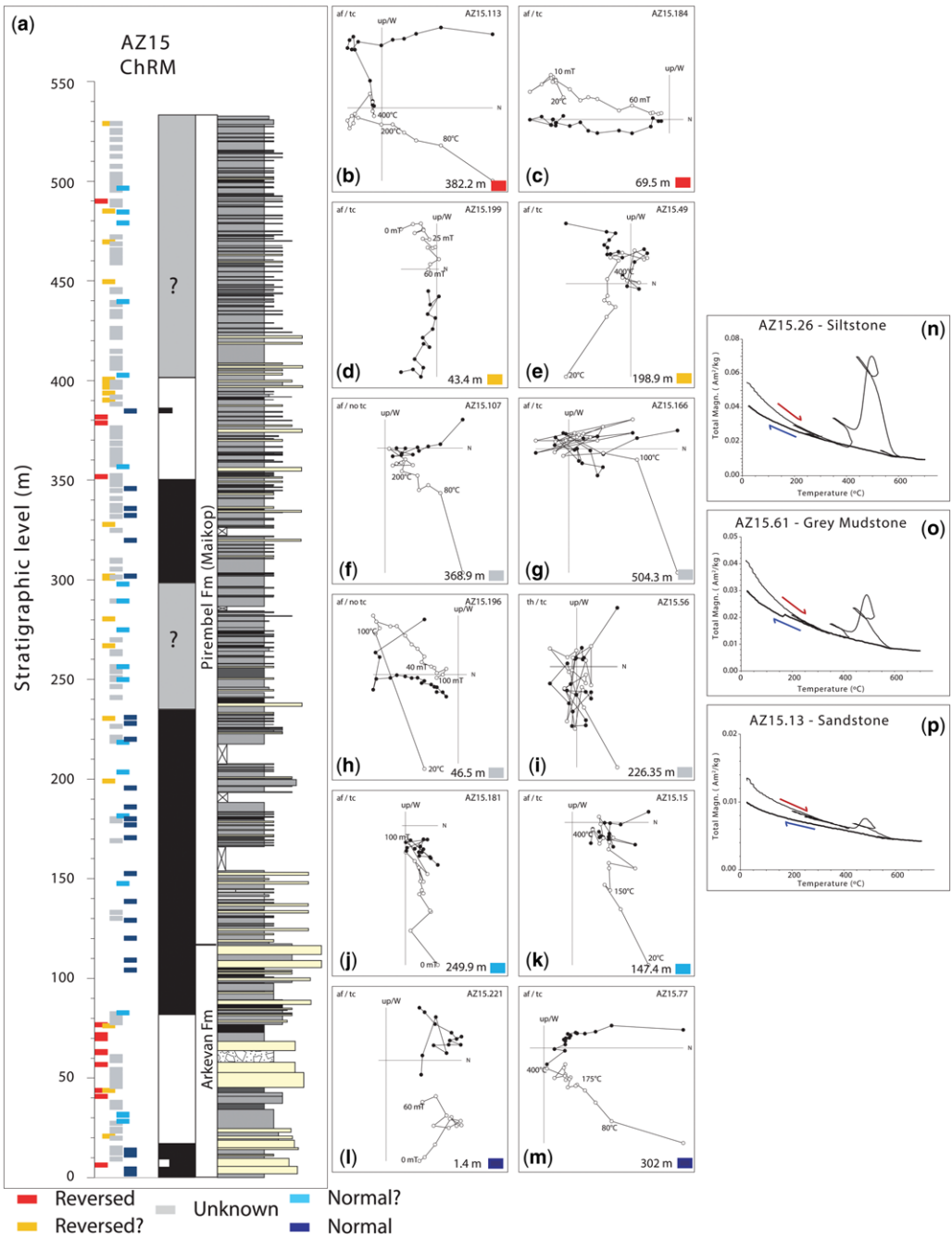
Fig. 6. Interpretation and examples of characteristic remanent magnetization directions (ChRM) of AZ15 and Curie balance results. (**a**) Lithostratigraphic log of section AZ15 and interpretation of characteristic remanent magnetization. (**b**–**m**) Examples of samples that were assigned a reversed (**b**, **c**), reversed? (**d**, **e**), unknown (**f**, **g**, **h**, **i**), normal? (**j**, **k**), normal (**l**, **m**) polarity. (**n**–**p**) Curie balance results of samples of different lithologies: (**n**) siltstone; (**o**) grey mudstone; and (**p**) sandstone.
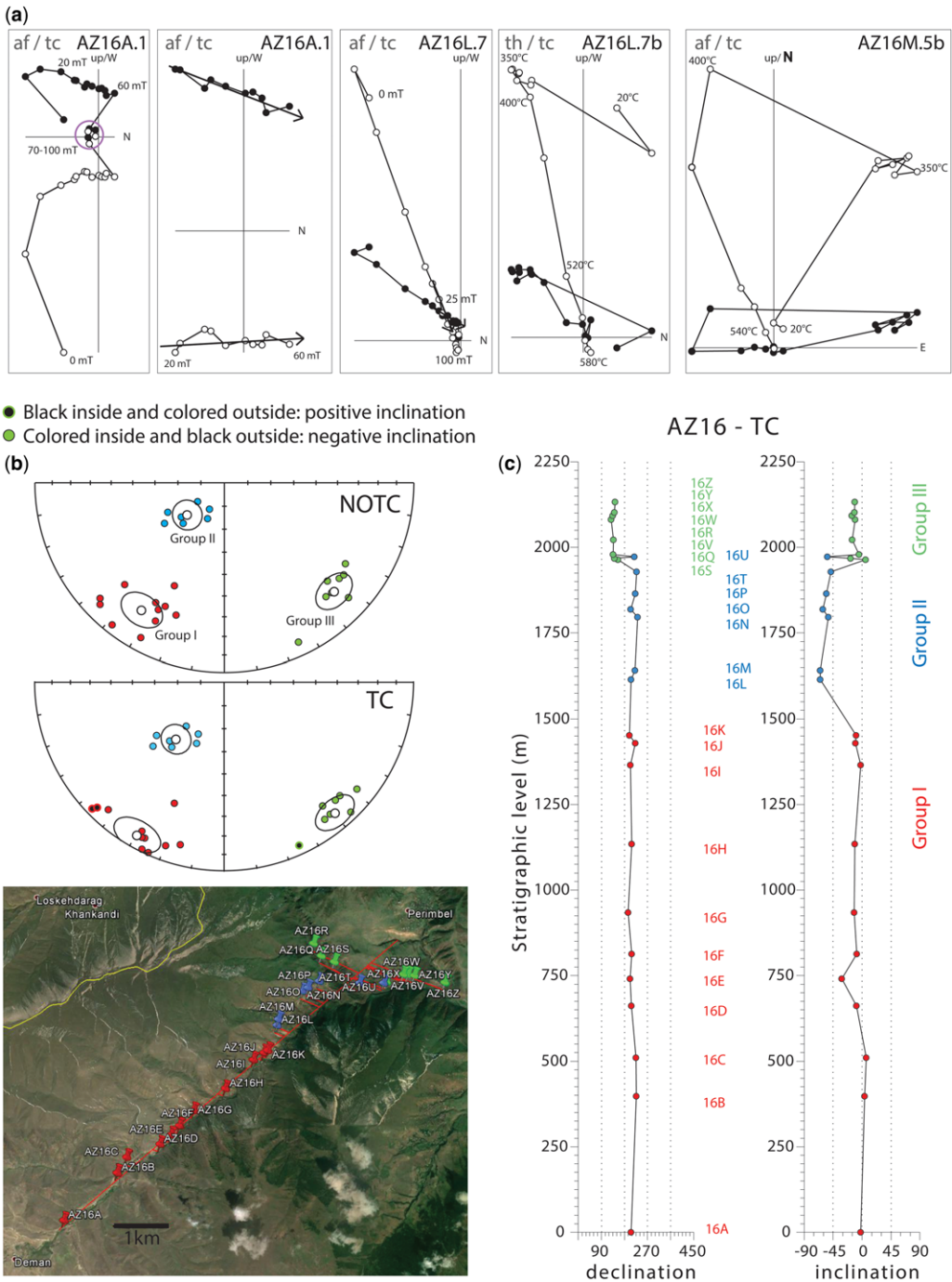
Fig. 7. Interpretation and examples of characteristic remanent magnetization directions (ChRM) of AZ16. (**a**) Zijderveld diagrams of samples with arrows showing interpreted components of alternating field demagnetized samples. Thermally demagnetized sample Zijderveld diagrams are shown for comparison. (**b**) Averages of interpreted declination and inclination per cooling unit in an equal area diagram. Three groups are apparent that match the stratigraphy of the sampled cooling units. A satellite image (Google Earth) of the location of cooling units is also shown. (**c**) Average declination and inclination v. the stratigraphic position for each cooling unit.

Fig. 8. (**a**) $^{40}Ar/^{39}Ar$ age spectrum, K/Ca ratios and radiogenic $^{40}Ar^*$ contents for all heating steps. Width of box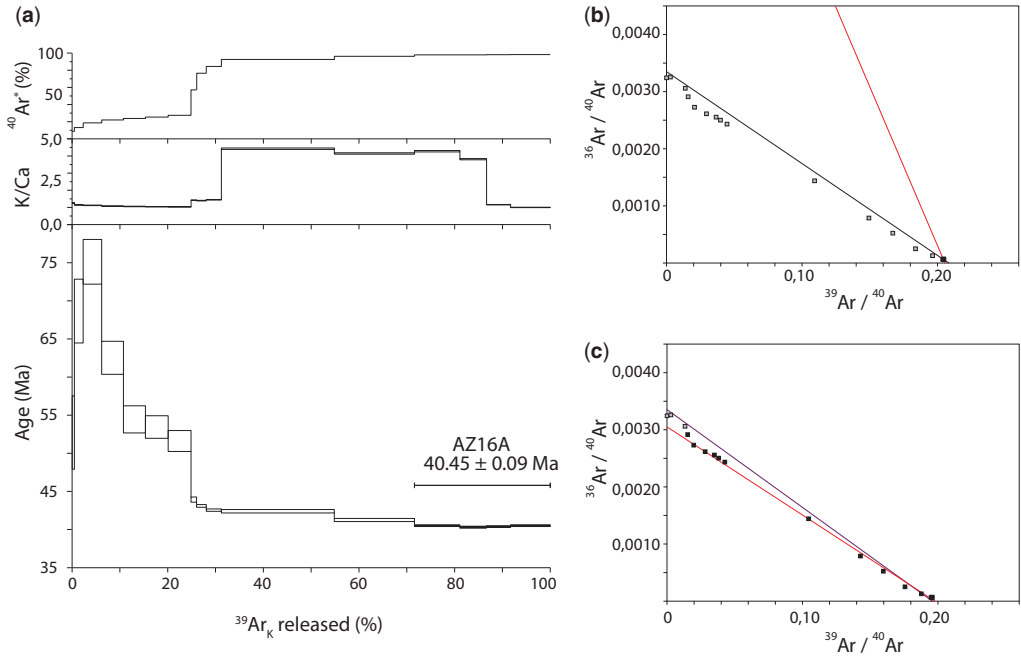es represents 2σ analytical uncertainty. (**b**) Inverse isochron of steps included in the plateau. Red line is isochron, black line is reference line going through the atmospheric $^{40}Ar/^{36}Ar$ intercept. (**c**) Inverse isochron of steps containing >10% radiogenic $^{40}Ar^*$ (see text for discussion).

reversals. The basal part of the section shows dominantly normal polarities and a normal/reverse (R/N) polarity transition at 17 m. The next R/N transition occurs at 82 m, in the upper part of the Arkevan formation. Another N/R reversal occurs in the Pirembel formation at 350 m.

Volcanic rocks of the Peshtasar formation (AZ16). Specimens from all 26 levels were demagnetized using AF demagnetization up to 100 mT. Additional thermal demagnetization was applied to two specimens per level. The results of the AF and thermal demagnetization (Fig. 7a) are very similar. Many cooling units have multiple components; a low coercivity or low temperature component is usually removed after demagnetization up to 20 mT or 200–250°C. We consider this to be a viscous overprint, which is usually randomly directed and occasionally carries the present-day field. In the majority of the samples a ChRM has been interpreted that was typically removed between 20 and 60 mT or between 300 and 500°C (Fig. 7a). For each level (or cooling unit) we calculated the Fisherian mean directions (Fig. 5). Some levels show a fairly large scatter with a precision parameter (*k*) lower than 50 (5/26 sites). This may result from the fact that

we measured more than a single spot-reading of the field by sampling more than a single cooling unit. From thin sections it appears that a number of levels represent sills (Van der Boon 2013). The generally slower cooling rate of shallow intrusive rocks may therefore result in a longer record of the magnetic field. We have plotted the mean ChRM for all sampled levels in AZ16 in Figure 7. Occasionally, the samples contained a high coercivity/temperature component observed above 60 mT or 500°C, of which the character remains elusive.

When we considered all the ChRM directions from AZ16, it became evident that there were three distinct directional groups. These palaeomagnetic groups coincide with equally distinct groups in the stratigraphic order in the sampled sequence (colour-coded in Fig. 7b). The lower group (I) contains units A–K and the middle group (II) contains units L–P, T and U. The upper group (II) contains units Q–S and V–Z. According to the stratigraphic order, unit U belongs to group III, whereas it clearly belongs palaeomagnetically to group II. There is, however, very little stratigraphic distance between the flows in this interval and we sampled partly along-strike (see Fig. 7b). Therefore a slight unnoticed change in the lateral variation in the thickness
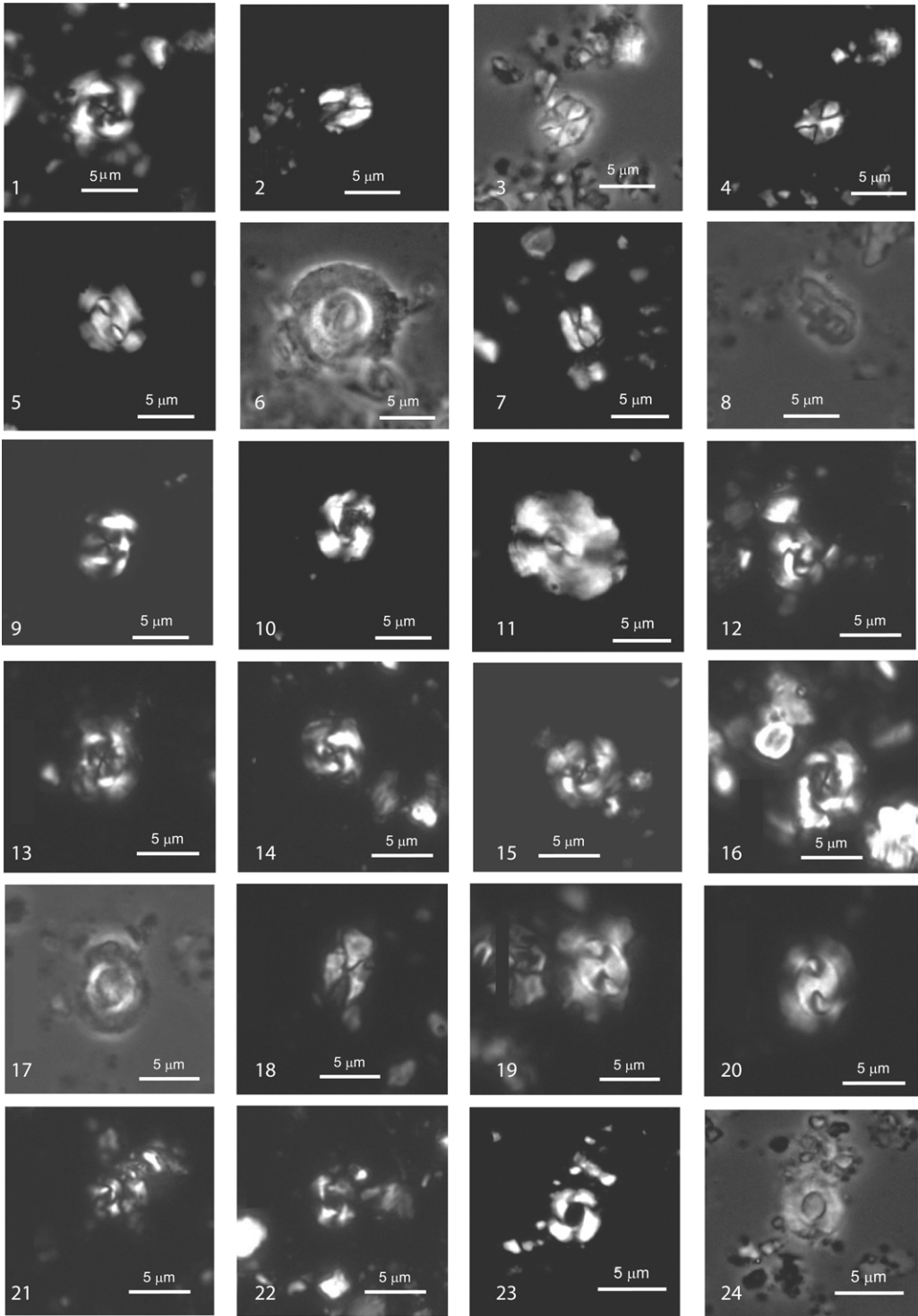
of the flows or the presence of sills can lead to a relative stratigraphic position of U in the upper group (II) instead of the middle group (III).

The present-day inclination of the region is approximately 58°. Little northward movement since the Eocene is expected, so the Eocene values should be roughly similar. The palaeomagnetic directions before tilt correction are very shallow for groups I and III (inclination $-20.8°$ and $-19.5°$, respectively) and rather steep for group II (inclination $-68.8°$). A striking feature is that the tilt correction (as derived from the sedimentary beds below, within and above the volcanic sequence) causes the directions to become shallower. We are therefore not certain that tilt correction is warranted. This would apply especially to the sills that form the majority of the volcanic rocks in the sequence. It is unlikely that the mean ChRM directions of the three groups are caused by remagnetization because this would have led to similar directions for all three groups.

More striking is the large dispersion of the three groups, which is not often recorded as a result of palaeo-secular variation. We notice, however, that similar groups – each forming a rather tight cluster – with such a wide dispersion have been observed in Central Atlantic Magmatic Province lavas of Early Jurassic age in the High Atlas and the Argana Basin in Morocco (Deenen *et al.* 2011*a*; Knight *et al.* 2004).

$^{40}Ar–^{39}Ar$ dating

Some of the cooling units that we aimed to date had already been analysed by Vincent *et al.* (2005) and can be directly compared with our data when the $^{40}Ar/^{39}Ar$ ages are recalculated using the calibration model of Kuiper *et al.* (2008). The lowermost cooling unit AZ16A is very close to sample TA92.6 of Vincent *et al.* (2005) with a recalculated age of 41.0 Ma (reported age 40.5 Ma). In the top part, AZ16Y is close to sample TA87.1 with a recalculated age of 38.8 Ma (reported age 38.3 Ma). Unfortunately, we were not able to analyse most of our samples because of the presence of large amounts of excess argon. Even very small heating increments (0.1% increase in laser power of a 50 W continuous wave CO_2 laser) yielded ^{40}Ar signals higher than our analytical range. Therefore we decided to heat our samples with 5% of the total laser power of 50 W and pump the released gas directly away. Groundmass samples have usually already released substantial amounts of $^{39}Ar_K$ at this laser power, but the size of the ^{40}Ar signals remained too high for analysis even after this step. Of 15 experiments, only unit AZ16A yielded an age spectrum. AZ16A (Fig. 8) shows a decreasing age spectrum. The four highest temperature steps show high amounts of radiogenic $^{40}Ar*$ ($>97\%$) and yield a weighted mean age of 40.45 ± 0.19 Ma (external uncertainty). However, these steps only comprise 28% of the released $^{39}Ar_K$. The K/Ca spectrum indicates the release of $^{39}Ar_K$ from different phases during heating. Furthermore, a reliable inverse isochron cannot be defined based on these high $^{40}Ar*$ steps (Fig. 8b), but an isochron including all steps $>10\%$ $^{40}Ar*$ shows indications of excess argon (Fig. 8c). Overall, it must be concluded that we were not able to produce reliable ages for the Peshtasar series. We can give a maximum age estimate of 40.45 ± 0.19 Ma only for AZ16A, which is in good agreement with the recalculated age of 41.0 Ma (reported age 40.5 ± 0.1 Ma) of Vincent *et al.* (2005).

Biostratigraphy

Twenty samples from section AZ15 were analysed for dinoflagellate biostratigraphy; all the samples were barren. Twenty-five samples were analysed for nannofossils, 14 of which were barren. The sampled levels are shown in Figure 4, with the light grey samples being barren of nannofossils.

Calcareous nannofossils. This assemblage is extremely scarce and preservation is moderate to poor. The most significant species useful for biostratigraphic assignment are *Cribrocentrum erbae, Isthmolithus recurvus* and *Cribrocentrum reticulatum.* Using these markers, the section can be placed within zones CNE 17 and CNE 19 of the biozonation of Agnini *et al.* (2014). The rare presence of *C. erbae* does not allow recognition of the acme of this species that defines the base and top of the CNE17 Zone, which otherwise is proposed as the best nannofossil bioevent to mark the base of the Priabonian (Agnini *et al.* 2011).

Fig. 9. Photographs of calcareous nannofossils. (**1**) *Cribrocentrum reticulatum,* crossed nicols (XN), 1250×, sample AZ15.46; (**2**) *Lanternithus* sp., XN, 1250×, sample AZ15.46; (**3, 4**) *Lanternithus* sp., CF (phase contrast), XN, 1250×, sample AZ15.46; (**5**) *Dictyococcites bisectus*, XN, 1250×, sample AZ15.46; (**6**) *Ericsonia formosa*, CF, 1250×, sample AZ15.46; (**7**) *Lanternithus* sp., XN, 1250×, sample AZ15.46; (**8**) *D. bisectus*, XN, 1250×, sample AZ15.103; (**9**) *Dictyococcites bisectus*, XN, 1250×, sample AZ15.103; (**10**) *Reticulofenestra dictyoda*, XN, 1250×, sample AZ15.131; (**11**) *D. bisectus* XN, 1250×, sample AZ15.177; (**12**) *Cyclicargolithus floridanus*, XN, 1250×, sample AZ15.46; (**13–16**) *C. reticulatum*, XN, 1250×, sample AZ15.46; (**17**) *C. reticulatum,* CF, 1250×, sample AZ15.46; (**18**) *Lanternithus* sp*.*, XN, 1250×, sample AZ15.46; (**19, 20**): *D. bisectus*, XN, 1250×, sample AZ15.46; (**21, 22**) *Reticulofenestra* sp., XN, 1250×, sample AZ15.46; (**23, 24**) *Reticulofenestra dictyoda,* XN, CF, 1250×, sample AZ15.146.

The presence of rare *I. recurvus* in few samples from 369.85 m is indicative of Zone NP 19 of Martini (1971) in the Priabonian. *Cribrocentrum reticulatum* is distributed from the lowest fossiliferous sample up to 500 m; its highest occurrence defines the top of CNE 19 of Agnini *et al.* (2014) dated at 35.24 Ma. Therefore the section is included in the interval spanning from Zone CNE17 to CNE19, which is correlated with Chrons 17n.2n to C15r.

Microphotographs of the most significant species are shown in Figure 9 and the results are summarized in Figure 10.

Large benthic forams. Several large benthic forams were found in the thick sand beds at the top of the Arkevan formation in section AZ15 (at *c.* 104 m). The following species were recorded: striate, small *Nummulites* sp., *Nummulites fabianii, Operculina* sp., *Orthophragminids* sp. and *Heterostegina reticulata.* Of these, the orthophragminids, *N. fabianii*, and *H. reticulata* all became extinct at the Eocene–Oligocene boundary. *Nummulites fabianii* is a marker for SBZ19–20 (Serra-Kiel *et al.* 1998), but it is difficult to separate it from its ancestral species. From the four specimens of *H. reticulata* it was possible to obtain details of the internal characteristics that are often used as stratigraphic indicators. The observed proloculus size ranged from 100 to 130 μm and the number of chambers without subdivision from three to four. This compares with similar characteristics seen in populations from the Vedi area in Armenia reported by Less *et al.* (2008). Photographs of the three species are shown in Figure 11. Uncertainty in the correlation of the SBZ biozones to the geological timescale or other biostratigraphic schemes (e.g. planktonic forams; Wade *et al.* 2011) prevent a more detailed age assignment than the early part of the Late Eocene. The best preserved specimen is an *Operculina* sp. (Fig. 11), which is an extremely long-ranging taxon. The large benthic forams do not show indications of mixing in the sense of the overlapping ranges of the present species. However, reworking might be an issue, as some of the grains are rather coarse and sands are not indicative of a typical large benthic foram environment.

Geochemistry

The generally low LOI, between 0.65 and 1.99 wt%, indicates that the samples were fresh. Four samples showed LOI values of 2.90, 2.33, 2.04 and 2.06 wt%. However, these values are still within the range of samples that are considered suitable for geochemical analyses (e.g. Handley *et al.* 2007).

The XRF results show that all the samples were very similar in chemical composition (Table 1). According to the IUGS classification of alkaline rocks, the samples are trachybasalts and basaltic trachyandesites. The samples have no normative

	Sample	Stratigraphic position (m)	*C. pelagicus*	*C. erbae*	*C. reticulatum*	*C. floridanus*	*D. bisectus*	*D. scrippsae*	*D. saipanensis*	*E. formosa*	*I. recurvus*	*L. cf. arcanus*	*Lanternithus* sp.	*L. minutus*	*Reticulofenestra* sp.	*R. dictyoda*	*R. daviesi*	*R. samodurovii*	*R. umbilicus*	*Sphenolithus* sp.	*S. cf. radians*	*T. pulcher*	*Z. bijugatus*	Reworked Cretaceous taxa	Okada & Bukry (1980)	Martini (1971)	Agnini *et al.* (2014)
AZ	MP 10	531																									
AZ	15,177	529.5	x			x									x												
AZ	15,164	501.9	x			x									x	x											
AZ	MP 9	500	x		x	x	x	x		x	x	x					x								CP 15b	NP 19-20	CNE 18-19
AZ	15,146	459.4																									
AZ	MP 8	458																									
AZ	15,131	422.1													x												
AZ	15,120	397.3																									
AZ	MP 7	389	x		x			x		x	x				x		x	x									
AZ	15,103	360.85				x					x				x					x							
AZ	MP 6	352																									
AZ	15.81	320.3	x		x		x			x			x					x	x			x	x	CP 15a	NP 18	CNE 18-19
AZ	15.75	301.25																									
AZ	MP 5	290																									
AZ	MP 4	261																									
AZ	15.50	203.8																									
AZ	15.46	186.2	x		x	x	x		x			x		x					x								
AZ	MP 3	180			x		x							x											CP 15a	NP 18	CNE 18-19
AZ	15.15	147.4																									
AZ	MP 2	134			x				x			x						x			x						
AZ	15.7	104.25																									
AZ	MP 1	76	x	x	x	x		x											x			x		CP15a	NP18	CNE 17
AZ	15,184	69.5																									
AZ	15,204	31.8																									
AZ	15,213	13.4																									

Fig. 10. Range chart of nannofossil taxa present in section AZ15.

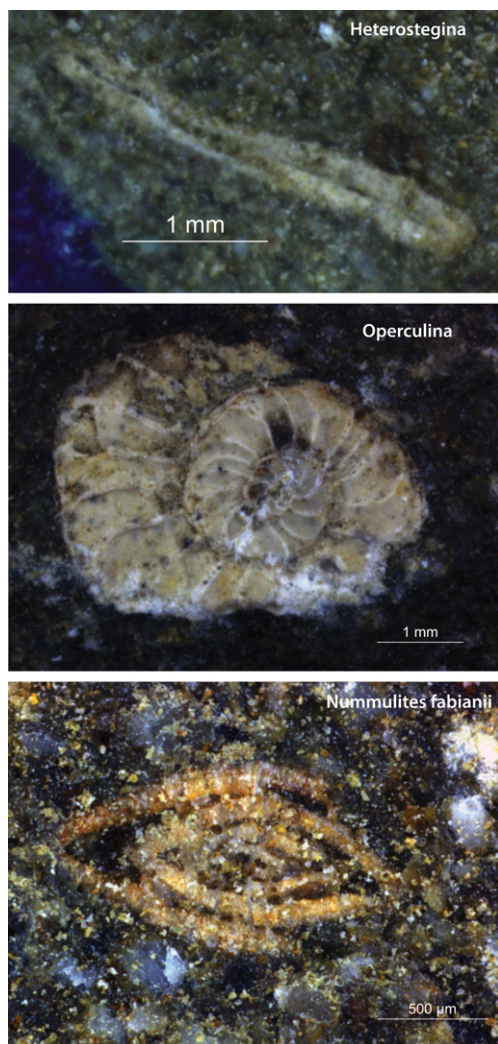**Fig. 11.** Photographs of large benthic foraminifera of AZ15.

quartz, low Fe enrichment, a high alkali content ($Na_2O + K_2O > 5\%$), high K_2/Na_2O, and are enriched in P, Rb, Sr, Ba, Pb and light rare earth elements. Furthermore, the samples show a low TiO_2 (<1.3%) content and have a high, variable Al_2O_3 (14–19%) content. Thus the samples show shoshonitic compositions (Morrison 1980). The samples do not show a trend in major element composition because the trends (plotted either v. SiO_2 or stratigraphic level) of all the major elements are generally flat (see Fig. 12a).

The N-MORB normalized spider diagram (see Fig. 12c) shows that (compared with the average N-MORB; Sun & McDonough 1989), all samples exhibit an Nb trough, a Th spike, an enrichment in the LILEs (Rb, Ba, K, Pb and Sr) and a relative depletion in heavy rare earth elements (Dy, Y, Er and Yb).

Samples from AZ14 and AZ16 plot within the same reach and we can therefore assume that they represent the same formation, which is consistent with the observations of Vincent *et al.* (2005). Notably, the three groups that were observed in AZ16 in terms of magnetic signal are also observed in the plots of many elements and even more so from ratios. However, they are most clear in the plots of metals such as Th, U, Zr and Nb when plotted v. SiO_2 content (see Fig. 12b for the example of Th). From these plots we concluded that the volcanic rocks from AZ14A and AZ14B belong to the middle unit (II) of section AZ16. Furthermore, AZ14C, AZ14D and AZ14F belong to the upper unit (III) of section AZ16. Sample AZ16A is an outlier in many geochemical plots. This lowermost flow was sampled just above the sands of the Neslin formation, so it might have experienced some crustal or sediment contamination.

Discussion

Onset of Maikop sedimentation in the Talysh Mountains

In the Talysh Mountains, the onset of the Maikop Series is marked by the Arkevan–Pirembel transition, located at the level of 118 m in section AZ15. The Arkevan–Pirembel transition occurs in the second interval of normal polarity. Our interpretation of the combined palaeomagnetic and biostratigraphic dataset correlates the lowest reversed interval to C17n.1r (Fig. 13), as this is the only reversed interval within CNE17. This yields an age for the corresponding stratigraphic level at the R/N transition (at 82 m) of 37.8 Ma. The base of common *I. recurvus* occurs within Zone CNE18 in the upper part of upper Chron C17n.1n (Fornaciari *et al.* 2010) or in the lowermost part of Chron C16n.2n, thus it straddles Chron C16r (Agnini *et al.* 2014). In our AZ15 record, *I. recurvus* first appears in samples 15.103 and MP7, which correspond to a reversed polarity interval. Consequently, we consider it most likely that the N/R polarity transition at *c.* 350 m correlates to the base of Chron 16r at an age of *c.* 37 Ma. It should be noted, however, that we cannot fully exclude alternative correlations as the distribution of the calcareous nannofossil marker species theoretically spans the interval from Zones CNE17 to CNE19, which are correlated with Chrons 17n.2n to C15r.

There is roughly 270 m of stratigraphy within the interval between these polarity transitions, leading

Table 1. *Geochemistry results*

Sample	AZ14A	AZ14B	AZ14C	AZ14D	AZ14F	AZ16A	AZ16B	AZ16C	AZ16D	AZ16E	AZ16F	AZ16G	AZ16H	AZ16I	AZ16J
Setting	Sill	Sill	Sill	Sill	Flow	Flow	Flow	Sill	Sill	Sill	Sill	Sill	Sill	Flow	Flow
Major elements (wt%)															
Fe_2O_3	9.27	8.44	9.97	9.54	8.48	8.34	8.84	8.56	8.94	8.84	8.81	8.86	8.54	8.63	8.75
MnO	0.15	0.18	0.18	0.16	0.15	0.15	0.16	0.16	0.17	0.16	0.16	0.16	0.12	0.16	0.14
TiO_2	1.12	1.12	1.12	1.08	1.20	1.10	0.96	0.97	0.99	0.98	0.99	0.98	0.99	0.96	0.98
CaO	8.25	8.51	8.61	8.13	7.93	8.27	8.32	8.33	8.31	8.26	8.55	8.37	8.70	8.59	8.42
K_2O	3.17	3.18	2.77	3.19	3.17	3.04	2.87	3.15	2.98	3.15	2.93	2.93	2.96	2.89	2.85
P_2O_5	0.47	0.47	0.46	0.43	0.48	0.37	0.36	0.37	0.38	0.36	0.37	0.37	0.37	0.36	0.36
SiO_2	52.34	52.38	50.48	50.55	51.13	52.61	51.66	52.79	51.95	52.27	51.92	51.96	52.58	52.45	52.12
Al_2O_3	17.70	17.53	16.92	16.06	18.04	16.98	16.03	16.64	16.18	16.12	16.24	16.57	17.04	16.52	16.21
MgO	4.83	4.48	6.71	6.72	5.46	4.67	6.54	6.18	6.35	6.35	5.73	5.78	4.88	6.30	6.25
Na_2O	2.95	2.94	2.55	2.82	2.73	2.91	2.76	2.88	2.79	2.81	2.61	2.79	2.88	2.82	2.87
BaO	0.08	0.08	0.07	0.11	0.15	0.07	0.07	0.08	0.07	0.08	0.08	0.07	0.08	0.07	0.08
LOI	1.40	1.12	1.99	2.90	2.33	1.08	0.65	0.83	0.74	0.89	1.42	0.89	1.07	0.70	0.65
Total	100.33	99.31	99.83	98.78	98.93	98.50	98.55	100.103	99.10	99.38	98.39	98.86	99.15	99.76	99.01
Trace elements (ppm)															
Ba	684.96	694.62	645.38	984.51	1374.29	624.07	669.58	697.60	670.95	687.95	683.58	680.80	681.68	674.46	670.86
Ce	70.80	69.11	55.08	56.00	64.27	87.90	63.54	65.59	65.65	63.28	64.64	66.25	68.10	67.49	66.66
Co	26.91	28.51	32.77	34.25	29.97	29.28	30.82	28.45	29.76	30.11	30.62	28.72	28.98	28.86	29.56
Cr	163.33	176.77	235.12	243.82	287.19	173.55	283.34	250.22	271.28	258.78	267.57	240.79	257.54	242.86	329.55
Cu	99.99	100.28	95.40	69.05	107.46	70.55	64.94	59.69	69.26	58.90	54.20	64.55	66.70	61.14	62.54
Dy	5.71	6.13	4.45	5.66	4.31	4.19	5.20	3.36	3.01	2.96	4.10	2.06	4.50	4.55	2.85
Er	2.80	2.69	2.45	2.58	3.13	3.13	2.87	2.51	3.22	2.42	2.64	2.86	3.50	2.99	2.62
Ga	19.00	19.22	17.80	16.40	20.12	18.91	17.62	17.96	17.77	17.63	17.88	18.02	18.66	17.79	17.76
Hf	5.10	5.21	4.52	5.00	4.80	7.54	5.73	5.07	5.26	5.58	5.60	5.45	5.78	6.03	5.31
La	36.22	37.02	29.46	29.62	37.75	47.48	35.09	35.65	34.18	33.71	35.32	37.32	36.89	35.28	36.26
Mo	2.49	2.18	1.82	1.10	0.88	2.55	1.94	1.83	2.12	2.02	3.15	2.10	2.24	1.96	1.96
Nb	20.72	21.20	14.60	14.80	17.00	29.48	20.10	20.27	20.14	20.40	20.68	20.06	20.53	20.11	20.71
Nd	33.29	30.49	28.42	21.63	28.06	39.63	29.79	30.02	32.58	25.09	28.92	33.02	30.09	30.46	32.11
Ni	65.18	70.57	88.47	95.90	93.82	77.97	89.29	78.37	86.47	84.89	87.22	80.75	86.42	80.82	79.78
Pb	19.74	17.74	12.10	9.77	13.07	14.16	13.90	12.39	11.41	10.79	6.86	15.29	28.89	14.01	19.22
Pr	8.72	8.27	7.04	6.32	8.00	10.71	7.88	7.91	8.10	6.90	7.79	8.79	8.28	7.97	8.30
Rb	84.10	81.67	70.08	71.07	69.67	93.04	65.44	91.94	92.89	95.47	79.82	85.46	84.05	80.56	66.49
Sc	23.51	24.55	24.41	23.01	27.11	23.61	24.45	23.71	22.65	22.70	24.96	23.01	22.85	24.12	24.43
Sm	5.69	5.31	5.00	4.30	5.27	6.26	5.21	5.00	5.51	4.42	4.97	5.84	5.27	5.25	5.51
Sr	554.34	564.57	578.39	1055.45	606.34	527.79	598.53	596.12	579.58	580.91	576.70	596.24	649.11	608.09	605.15
Ta	0.38	1.47	0.60	2.19	2.13	1.69	2.21	0.72	1.48	1.23	1.81	1.94	1.49	0.72	1.24
Th	10.67	10.47	6.40	7.12	7.36	22.24	12.71	12.48	13.08	12.87	13.15	13.04	13.10	12.91	13.11
U	2.77	2.47	0.86	1.04	1.85	6.23	3.10	3.05	3.48	3.60	3.23	3.29	3.24	2.95	2.79
V	209.51	216.47	237.78	239.05	266.82	194.12	198.73	190.34	196.60	190.10	200.12	195.36	195.71	189.20	197.08
W	4.25	3.54	2.25	1.75	2.16	4.39	4.95	5.09	7.19	6.26	4.39	5.17	4.43	3.47	3.54
Y	25.35	25.28	22.59	20.88	24.43	28.42	23.87	23.91	24.10	24.04	24.52	23.99	24.16	23.92	24.16
Yb	2.38	2.90	2.57	2.32	2.65	2.90	2.37	2.14	2.18	2.49	2.48	2.19	2.81	3.03	2.82
Zn	84.82	90.12	78.37	70.44	98.18	89.13	88.07	74.01	77.90	78.14	73.36	84.26	89.55	80.71	90.18
Zr	168.39	171.51	108.76	81.41	126.26	262.65	171.15	170.58	173.45	173.58	178.01	172.09	173.53	171.16	177.36

to an average sedimentation rate of approximately 34 cm ka^{-1}. Taking the sedimentation rate of 34 cm ka^{-1}, the age at the top of the sampled section can be calculated through extrapolation, leading to an age of around 36.5 Ma. The base of the section is similarly estimated at *c.* 38 Ma. Consequently, the whole section is estimated to cover the time span from approximately 38–36.5 Ma. The transition from the Arkevan formation to the Pirembel formation at 118 m is estimated at 37.7 Ma. Extrapolating the same sedimentation rate further upwards, the EOT should be expected at a height of 900 m above the top of our section. Vincent *et al.* (2005) mention a thickness for the entire Maikop Series in the Talysh Mountains of 1500 m, which suggests it should be almost entirely of Eocene age. The detailed overview of the stratigraphy of the Talysh by Vincent *et al.* (2005) does not report any

evidence for Oligocene fauna. A Late Eocene age for the base of the Pirembel formation is in agreement with the study of Amini (2006), which concludes that the Ojaghgeshlagh formation just across the border in Iran is equivalent to the Pirembel formation and starts during the Late Eocene.

The age of 37.7 Ma for the onset of Maikop sedimentation in the Talysh proves that it is not related to the major sea-level lowering at the EOT (33.9 Ma, Vandenberghe *et al.* 2012). The age instead indicates a tectonic cause, further evidenced by the end of a major episode of volcanism within the Arabia–Eurasia collision zone. This may also explain the younger ages for the onset of Maikop sedimentation in regions further away from the collision zone (Schulz *et al.* 2002; Sachsenhofer *et al.* 2009). The transition to anoxic conditions in the Paratethys is most probably a complex combination

AZ16K Sill	AZ16L Sill	AZ16M Flow	AZ16N Flow	AZ16O Flow	AZ16P Flow	AZ16Q Flow	AZ16R Flow	AZ16S Sill	AZ16T Flow	AZ16U Flow	AZ16V Flow	AZ16W Sill	AZ16X Flow	AZ16Y Sill	AZ16Z Flow
8.90	8.94	9.33	9.63	9.01	9.13	9.39	9.07	9.62	8.54	8.64	9.47	9.52	9.35	9.21	9.40
0.12	0.17	0.12	0.15	0.16	0.16	0.18	0.17	0.17	0.15	0.17	0.17	0.17	0.18	0.17	0.16
1.03	0.99	1.13	1.15	1.11	1.12	1.02	1.05	1.04	1.11	1.17	1.00	1.05	1.03	1.07	1.07
8.66	8.47	9.15	8.49	8.42	8.57	8.51	9.24	8.57	8.65	8.70	8.27	8.50	8.47	8.83	8.51
3.00	2.97	2.91	2.87	2.94	2.79	2.73	2.76	2.75	2.90	2.97	2.74	2.88	2.84	3.00	2.81
0.38	0.38	0.42	0.40	0.40	0.42	0.43	0.43	0.42	0.42	0.42	0.41	0.44	0.43	0.44	0.44
52.80	52.63	51.76	51.16	51.18	51.10	50.56	51.09	50.70	51.64	51.78	50.39	51.06	50.70	50.78	50.65
16.65	16.80	16.85	16.48	17.12	16.59	16.75	16.76	16.21	18.09	17.52	15.85	16.77	16.51	16.51	16.66
4.97	5.89	4.97	6.64	6.00	6.44	6.94	5.45	7.27	4.50	4.60	7.71	6.95	6.80	6.72	6.84
2.85	2.85	2.70	2.74	2.91	2.71	2.52	2.65	2.50	2.91	2.88	2.92	2.63	2.53	2.71	2.57
0.08	0.08	0.08	0.07	0.08	0.07	0.07	0.07	0.07	0.08	0.08	0.07	0.08	0.09	0.08	0.08
1.08	1.23	1.22	1.14	1.60	1.22	2.04	1.30	1.91	1.15	1.03	1.73	2.06	1.89	1.09	1.85
99.43	100.16	99.44	99.77	99.32	99.09	99.09	98.73	99.31	98.97	98.92	99.01	100.03	98.91	99.51	99.20
677.42	720.99	686.30	640.56	706.46	674.05	614.25	626.14	648.10	676.55	665.80	660.18	678.70	795.31	715.46	681.20
70.56	63.89	70.20	62.60	62.07	64.38	54.84	56.88	49.62	68.35	65.58	52.83	54.40	54.20	55.23	57.30
29.69	31.46	32.04	32.16	29.35	31.11	34.14	33.39	34.82	27.55	30.95	35.11	33.91	33.97	30.72	32.90
235.90	203.04	212.61	219.65	183.86	200.81	280.26	288.20	318.44	148.59	236.10	290.84	261.39	264.91	241.03	281.10
64.66	69.71	72.11	70.75	74.58	72.58	80.22	83.61	88.34	77.14	75.26	84.57	81.61	85.30	87.67	77.98
4.59	3.80	4.74	6.32	4.72	4.70	5.26	4.29	4.86	4.65	5.13	4.64	6.21	4.89	5.24	5.94
2.62	2.48	2.75	3.35	2.58	2.23	3.46	2.67	3.15	2.77	2.64	2.84	3.35	2.86	2.81	2.94
18.32	18.32	18.67	18.17	18.80	18.58	18.32	18.93	17.75	19.87	19.61	17.55	18.03	17.79	17.58	18.16
5.48	5.04	5.51	4.98	5.23	5.68	4.12	4.85	4.46	5.74	5.79	4.27	4.50	4.33	3.90	4.38
36.95	35.40	36.53	31.77	30.83	34.99	27.91	29.33	30.52	37.53	36.59	27.74	26.96	28.82	25.22	31.54
2.25	1.89	1.69	2.11	2.05	2.41	1.92	1.89	2.21	2.00	2.52	1.97	1.90	1.85	1.99	1.67
21.36	20.22	21.32	19.86	19.29	19.87	13.76	14.54	13.67	20.84	21.19	13.85	14.40	13.97	14.52	14.43
33.51	26.72	35.56	31.24	29.78	30.04	31.05	28.83	27.93	30.71	31.08	27.20	30.26	27.36	24.87	28.99
77.57	85.13	90.27	87.59	80.86	85.08	130.14	125.14	137.38	77.46	98.97	148.93	127.85	118.29	93.47	107.00
17.35	15.38	15.26	12.89	15.83	25.22	15.63	12.41	13.26	14.31	15.52	10.23	8.33	21.43	13.04	9.67
8.77	7.67	9.03	7.93	7.93	7.91	7.27	7.26	7.10	8.32	8.20	6.90	7.14	7.04	6.55	7.56
90.30	86.74	63.31	78.73	81.27	77.06	64.38	67.63	73.27	76.06	78.54	73.80	69.05	74.55	76.65	71.73
24.63	24.68	25.69	25.88	23.44	25.41	23.81	26.14	24.33	24.79	24.84	24.01	23.36	24.29	23.91	23.94
5.86	4.85	5.95	5.41	5.55	5.19	5.19	5.32	5.01	5.24	5.43	5.03	5.12	4.98	4.90	5.40
591.06	573.49	600.98	565.61	570.58	567.64	541.19	591.30	560.46	631.49	598.89	515.82	527.39	570.42	690.53	607.11
1.92	1.62	1.80	1.13	1.09	2.01	1.96	1.60	2.63	1.67	1.30	1.33	2.18	2.40	1.21	1.48
13.48	11.10	11.80	10.24	10.43	10.74	6.15	5.89	6.03	10.79	10.93	5.76	5.60	5.83	6.09	6.17
3.73	2.81	2.80	2.44	2.55	2.53	1.46	1.22	1.42	2.53	3.22	1.68	1.36	1.14	1.23	1.31
201.09	207.42	218.64	225.54	207.13	217.30	211.69	225.24	215.86	202.52	226.51	207.60	208.30	211.68	212.96	219.33
4.12	4.11	3.69	4.05	4.73	3.48	3.43	3.63	4.87	2.88	4.63	5.24	3.46	3.18	4.60	2.09
25.12	24.60	25.80	24.30	23.74	24.78	22.19	23.26	21.97	24.40	25.31	22.00	22.36	22.30	22.58	22.39
2.56	2.38	2.58	2.38	2.07	2.17	2.16	2.11	2.20	2.73	2.12	2.28	2.56	2.26	2.36	2.60
84.18	87.12	94.72	93.79	81.78	91.72	83.44	92.05	82.55	94.17	97.69	78.49	78.52	79.67	81.40	80.75
185.12	166.17	174.76	160.03	155.78	161.47	106.83	111.37	103.15	163.97	170.65	107.36	109.60	106.99	101.02	105.12

of regional tectonic activity and eustatic sea-level changes. For a better understanding of the controls on widespread anoxia in the Paratethys, the onset of Maikop sedimentation should be dated in high resolution in other regions. The question remains as to whether these sediments truly represent the equivalent of the Maikop sediments as stated in the studies of Azizbekov *et al.* (1979), Alizadeh *et al.* (2005) and Vincent *et al.* (2005).

Typical Maikop lithology is represented by laminated dark grey to dark brown clays, often containing jarosite and fish fossils (Saint-Germes *et al.* 2000; Hudson *et al.* 2008; Johnson *et al.* 2010). These characteristics are not observed in section AZ15 as these consist mostly of dark grey siltstones. Fish fossils and jarosite were not observed during our study. Stratigraphic correlation of the Maikop sediments in general is difficult, as there is an absence of levels that can be used as marker beds throughout the Eastern Paratethys. Coccolith-bearing limestone levels that are reported from the Western Paratethys (e.g. Haczewski 1996; Schulz *et al.* 2005; Ciurej & Haczewski 2012) are, to our knowledge, not reported from the Talysh.

Three volcanic episodes of the Peshtasar formation

Three groups are evident in the Peshtasar formation from a palaeomagnetic, stratigraphic and geochemical point of view. The palaeomagnetic results show that, within each group, there is dispersion that can be explained by secular variation based on the A95 values that fall within the N-dependent A95 envelope of Deenen *et al.* (2011b). Hence the three directional groups must each represent a
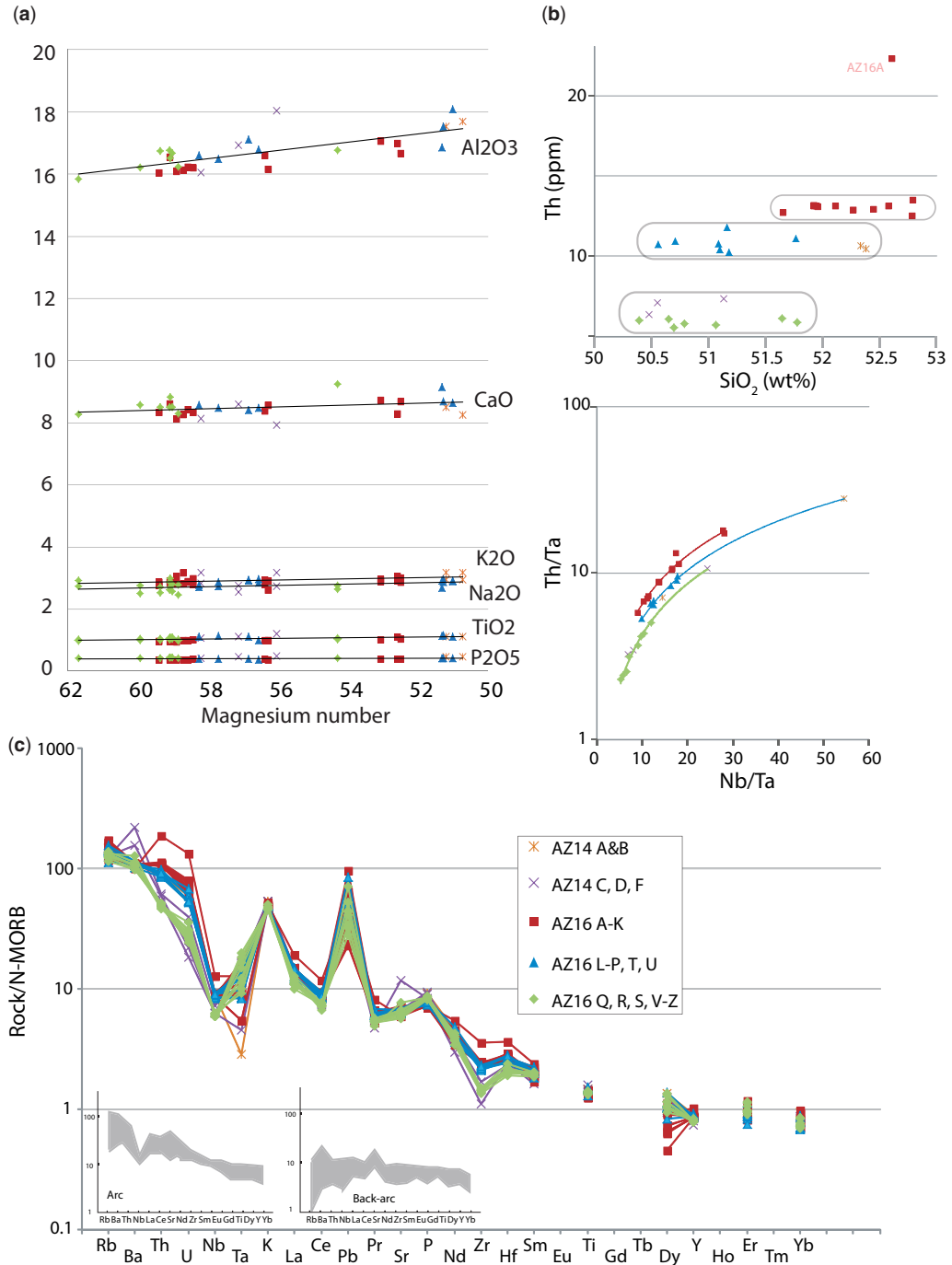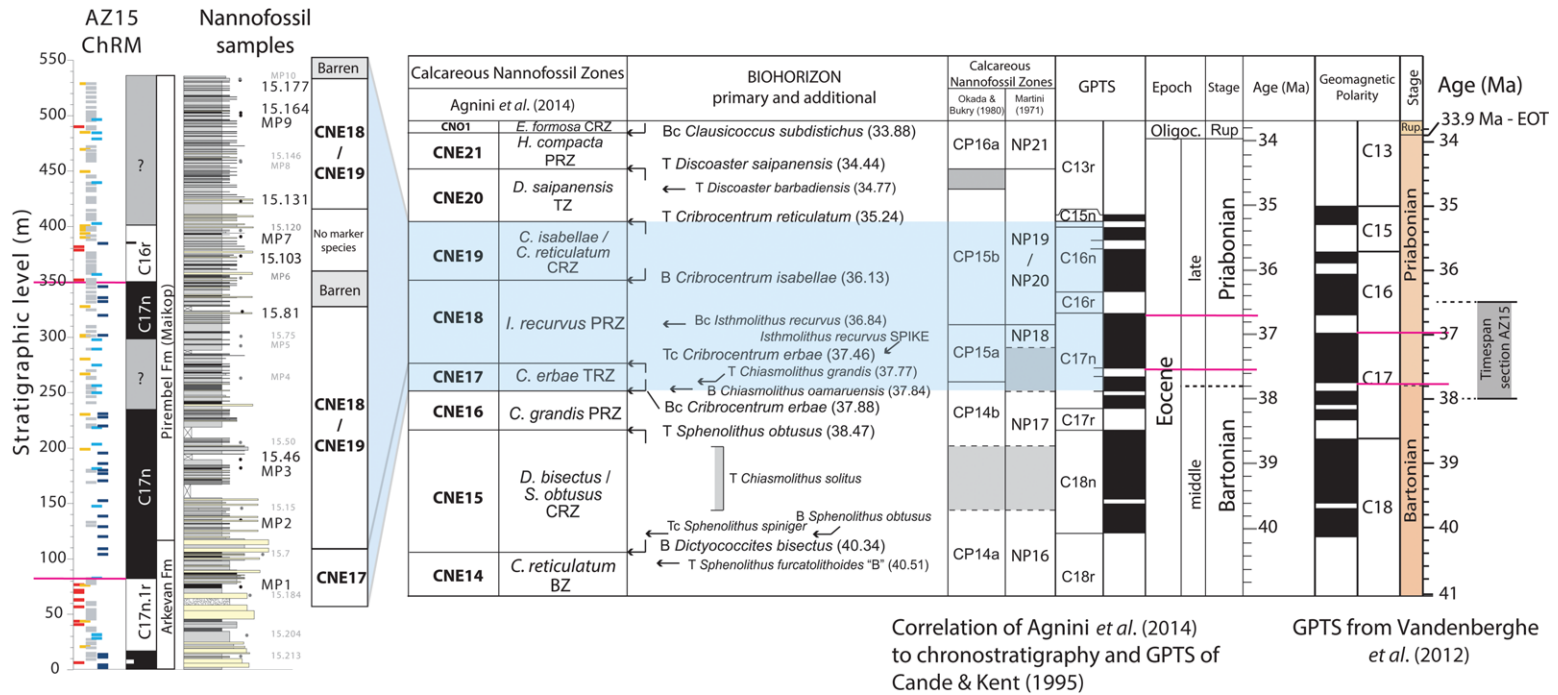
Fig. 12. Geochemistry results. (**a**) Weight percentage of oxides v. magnesium number (the ratio of magnesium to iron). Trends in this diagram are flat, indicating a lack of magma evolution. (**b**) Abundance of Th, which clearly shows three groups, as well as a plot of Th/Ta v. Nb/Ta. (**c**) Spider diagram, with arc- and back-arc compositions in grey (Pouclet *et al.* 1994).

Fig. 13. Magnetostratigraphy and nannoplankton correlation to the geological polarity timescale. The nannoplankton zones of Agnini *et al.* (2014) have been correlated with the polarity timescale of Cande and Kent (1995). Reversal ages have changed slightly for the polarity zones, according to the new the geological polarity timescale of Gradstein *et al.* (2012). This does not influence the correlation itself. For legend of palaeomagnetism, see Figure 6.
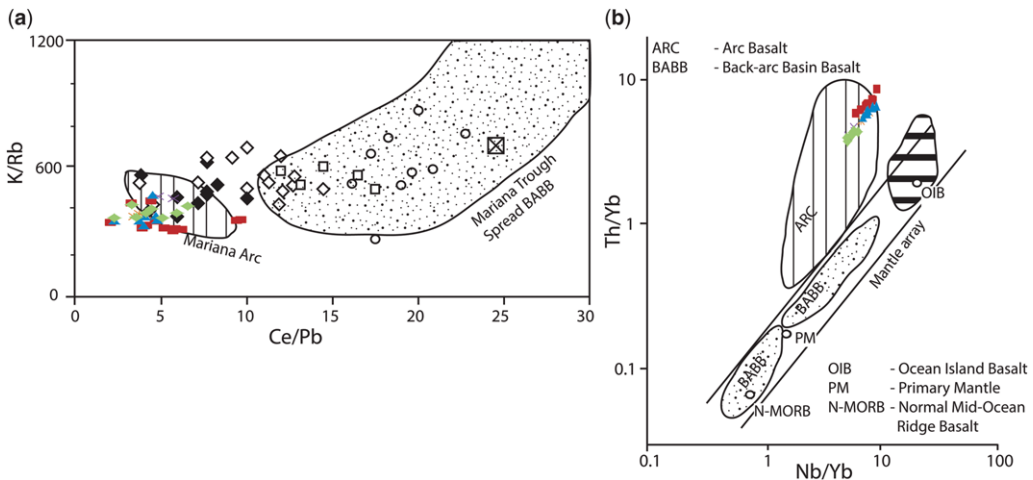
Fig. 14. (**a**) K/Rb v. Ce/Pb for the Mariana arc and back-arc compared with Gribble *et al.* (1998). (**b**) Th/Yb v. Nb/Yb compared with the Japan arc and back-arc of Pouclet *et al.* (1994). For legend of samples, see Figure 12.

period long enough (on the order of several kyr) to record some secular variation. Because the three groups yield very different mean ChRMs, it is unlikely that the Peshtasar formation was deposited by a process of uniform extrusion over 2 myr (based on the Ar–Ar ages of Vincent *et al.* (2005)). Instead, the Peshtasar formation was probably deposited during three short-lived magmatic pulses, with a maximum duration of several thousands of years, considering there is some secular variation in each group. This results in relatively high eruption rates because group I spans 1.5 km stratigraphically.

Arc volcanism in the Talysh

Magmas very rarely reach the surface without experiencing processes that modify their chemical composition. Magmas are usually affected by processes such as crustal assimilation, fractional crystallization and partial melting or magma mixing, processes that lead to evolved compositions. As all the trends of major elements in our observations of the Peshtasar lavas are almost flat (Fig. 12), these processes are unlikely to have severely affected the composition of the magma. This indicates a lack of magma evolution, which is consistent with the hypothesis that
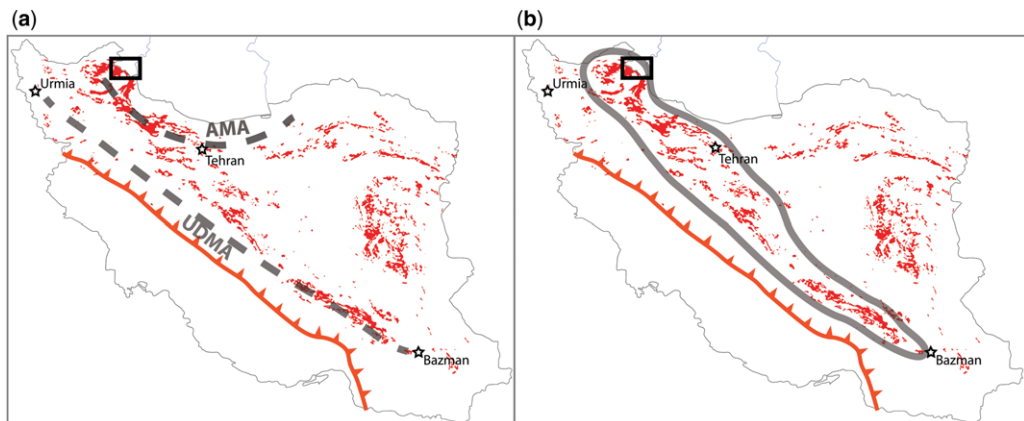
Fig. 15. Distribution of Eocene volcanic rocks in Iran (modified after Agard *et al.* 2011). (**a**) Locations of the Urumieh–Dokhtar Magmatic Arc (UDMA) and Alborz Magmatic Arc (AMA). (**b**) Our hypothesis in which Eocene volcanic rocks of the UDMA and AMA are part of one large belt. For legend, see Figure 2.

the three groups represent short-lived episodes of volcanism.

The N-MORB normalized trace element abundance patterns (see Fig. 12) of the samples are very similar to those of arc volcanoes found in other parts of the world (e.g. Handley *et al.* 2007). The anomalies in Nb, Ta and Zr are also clear evidence for magma generation related to subduction (Baier *et al.* 2008). Back-arc volcanism would potentially have the same signature (as back-arcs are always related to subduction). Back-arc basin basalt (BABBs) usually vary in geochemical composition anywhere between MORB-like signatures and arc-like signatures.

We compared our geochemical data with data from other arc/back-arc systems. In Figure 14a, the relevant trace element ratios (K/Rb and Ce/Pb) are plotted, together with data from the Mariana arc and the Mariana back-arc (Gribble *et al.* 1998). The Mariana arc was chosen because of the clear relative position of the arc and back-arc. Furthermore, late Cretaceous volcanism along the active margin of Eurasia had a geochemical signature resembling that of the Mariana arc (Kazmin *et al.* 1986). The comparison shows that all the samples fall entirely within the range of samples from the arc and none of the samples from the Talysh plots within the range of the Mariana back-arc. The Ce/Pb ratios may reflect a contamination with sediment, additional isotope studies are required for more insight into crustal contamination.

In Figure 14b, the ratios of Th/Nb v. Nb/Yb are plotted to compare different types of basalts (arc basalts, BABBs and oceanic island basalts) from the Japan Sea, in which the relative position of arc and back-arc is clear (Pouclet *et al.* 1994). The Peshtasar samples all plot in or near the ARC field, which are arc-like lavas (Pouclet *et al.* 1994), but none of our samples plots within the BABB fields.

The spider diagram patterns (Fig. 12) are characteristic of continental-arc basalts (Pouclet *et al.* 1994; Asiabanha *et al.* 2009; Verdel *et al.* 2011; Asiabanha & Foden 2012). Arc-like signatures have typical Nb troughs, Th spikes, LILE and Sr enrichment and relative HREE depletion. All the samples in this study exhibit these characteristics. Back-arc basin characteristics include a low LILE content, no Th anomaly and a flat REE pattern. None of the basalts in this study therefore represents BABBs in the geochemical sense. When the patterns are compared with the arc lavas and BABBs of Pouclet *et al.* (1994) (see Fig. 12c), they are much more similar to the arc lavas than the back-arc basalts. Spider diagrams from Asiabanha & Foden (2012), Vincent *et al.* (2005) and Verdel *et al.* (2011) show the same patterns (note that normalization with N-MORB or primitive mantle has little effect on the patterns). The scenario that Golonka

(2004) proposes, in which the volcanism of the Talysh and AMA is linked to ocean spreading in a back-arc basin, is therefore unlikely. These results are consistent with the continental-arc setting of the AMA as proposed by Asiabanha *et al.* (2009).

All the samples from the Peshtasar formation exhibit shoshonitic compositions. Shoshonitic compositions of Eocene volcanic rocks have also been reported from the UDMA and the NW of Iran (e.g. Torabi 2009; Dilek *et al.* 2010; Verdel *et al.* 2011). Shoshonites are usually found in (subduction-related) arcs, which often exhibit a progression along the tholeiite–calc-alkaline–shoshonite path. Shoshonites are generally formed later, stratigraphically higher and are associated with greater heights above the Benioff zone. Therefore they are usually found in mature arcs. In regions that are tectonically active and unstable, shoshonites are associated with deformation of the arc, near the termination of subduction, or when there is a transition between two subduction regimes that have a different orientation (Morrison 1980). Shoshonites are sometimes associated with slab break-off (Dilek *et al.* 2010; Verdel *et al.* 2011). It is possible that the shoshonites of the Talysh represent short-lived episodes of volcanism caused by the end of subduction or break-off of the Neotethys slab. This is in agreement with the scenario as proposed by Agard *et al.* (2011), which involves Paleocene–Eocene slab break-off, large shifts in arc magmatism and episodes in which upper crustal extension takes place.

Much controversy exists about the distribution of Eocene volcanic rocks in Azerbaijan and Iran. Many researchers infer the presence of two volcanic belts, the AMA (extending from the Talysh Mountains via the Alborz to the Kopet Dagh) and the UDMA (extending from near Lake Urmia to the SE of Iran) (Fig. 15a). These two belts do not entirely explain the distribution of the Eocene volcanic rocks, as they are lacking in parts of both the AMA and UDMA, especially in the regions near Urmia and east of Tehran (Fig. 15). Regarding the distribution patterns of Eocene volcanic rocks and geochemical arc signatures, we hypothesize that a different scenario may be plausible. The distribution of Eocene volcanic rocks can be traced almost continuously from the Talysh via the western part of the Alborz towards the southeastern part of Iran (Fig. 15b). In this scenario, Eocene volcanic rocks in the Kopet Dagh are not part of the same system, and may have different geochemical signatures.

Conclusions

We have used magnetostratigraphy and nannoplankton biostratigraphy to determine the age of the transition from the Arkevan formation to the

Pirembel formation. This transition has been assumed to represent the onset of Maikop sedimentation within the Talysh Mountains of Azerbaijan. A magnetostratigraphy was obtained for the upper part of the Arkevan formation and the lower part of the Pirembel formation, showing a polarity pattern of two normal and two reversed polarity intervals. This magnetostratigraphy was combined with a biostratigraphy based on nannoplankton assemblages that are characteristic for zones CNE17 and CNE18/19 (Late Eocene). The onset of Maikop sedimentation occurs in the lower part of C17n. 1n at an age of 37.7 Ma. The estimated sedimentation rate for the Late Eocene sediments of the Talysh is 34 cm kyr^{-1}, which suggests that Oligocene sediments are absent in the Talysh.

The onset of Maikop sedimentation in the Talysh started almost 4 myr before the occurrence of the EOT, which indicates a tectonic cause for the decrease in grain size observed at the Arkevan–Pirembel boundary. Also indicative of an active tectonic regime is the presence of approximately 2 km of subduction-related volcanic rocks of the Peshtasar formation, stratigraphically just below the Arkevan and Pirembel formations. The question remains whether the Pirembel sediments truly represent the equivalent of the classic Maikop Series that are deposited in the more distal parts of the Paratethys. Palaeomagnetic analyses of the volcanic rocks of the older Peshtasar formation in section AZ16 show three distinct groups that are also recognised as subsequent intervals in the stratigraphy. They are interpreted to represent three short time intervals (*c* 10^2–10^3 years), each interval recording some secular variation over a relatively short time. Deposition rates must have been very high because the lower group (I) has a stratigraphic thickness of 1.5 km. The three groups are also distinct in their geochemistry. Based on equal geochemical composition, we confirm the lateral relationship between the Arkevan and Peshtasar formations. Volcanic rocks of the Peshtasar formation are all trachybasalts and basaltic trachyandesites with trace element signatures characteristic of arc lavas. The volcanic rocks probably formed in a continental-arc setting. The major element geochemistry shows that the samples have shoshonitic compositions.

References

ABRAMS, M. A. & NARIMANOV, A. A. 1997. Geochemical evaluation of hydrocarbons and their potential sources in the western South Caspian depression, Republic of Azerbaijan. *Marine and Petroleum Geology*, **14**, 451–468.

AGARD, P., OMRANI, J. ET AL. 2011. Zagros orogeny: a subduction-dominated process. *Geological Magazine*, **148**, 692–725.

AGNINI, C., FORNACIARI, E. ET AL. 2011. Integrated biomagnetostratigraphy of the Alano section (NE Italy): a proposal for defining the middle-late Eocene boundary. *Geological Society of America Bulletin*, **123**, 841–872.

AGNINI, C., FORNACIARI, E., RAFFI, I., CATANZARITI, R., PÄLIKE, H., BACKMAN, J. & RIO, D. 2014. Biozonation and biochronology of Paleogene calcareous nannofossils from low and middle latitudes. *Newsletters on Stratigraphy*, **47**, 131–181.

ALIZADEH, A. A., AHMEDBEILI, F. S. ET AL. 2005. *Geological Map of Azerbaijan Republic 1:500,000*. National Academy of Sciences of Azerbaijan Republic, Geology Institute.

ALLEN, M. B. & ARMSTRONG, H. A. 2008. Arabia–Eurasia collision and the forcing of mid-Cenozoic global cooling. *Palaeogeography, Palaeoclimatology, Palaeoecology*, **265**, 52–58.

AMINI, A. 2006. Oligo-Miocene fluvial-dominated deltas on the shelf of the South Caspian Sea (Paratethys). *Facies*, **52**, 579–597.

ASIABANHA, A. & FODEN, J. 2012. Post-collisional transition from an extensional volcano-sedimentary basin to a continental arc in the Alborz Ranges, N-Iran. *Lithos*, **148**, 98–111.

ASIABANHA, A., GHASEMI, H. & MESHKIN, M. 2009. Paleogene continental-arc type volcanism in North Qazvin, North Iran: facies analysis and geochemistry. *Neues Jahrbuch für Mineralogie Abhandlungen*, **186**, 201–214.

AZIZBEKOV, S. A., BAGIROV, A. E., VELIEV, M. M., ISMAIL-ZADE, A. D., NIZHERADZE, N. S., EMELYANOV, E. N. & MAMEDOV, M. N. 1979. *Geology and Volcanism of the Talysh*. Elm, Baku [in Russian].

BAIER, J., AUDÉTAT, A. & KEPPLER, H. 2008. The origin of the negative niobium–tantalum anomaly in subduction zone magmas. *Earth and Planetary Science Letters*, **267**, 290–300.

BALLATO, P., UBA, C. E. ET AL. 2011. Arabia-Eurasia continental collision: insights from late Tertiary foreland-basin evolution in the Alborz Mountains, northern Iran. *Geological Society of America Bulletin*, **123**, 106–131.

BOWN, P. R. & YOUNG, J. R. 1998. Techniques. *In*: BOWN, P. R. (ed.) *Calcareous Nannofossil Biostratigraphy*. Kluwer Academic, London, 16–28.

BRUNET, M.-F., KOROTAEV, M. V., ERSHOV, A. V. & NIKISHIN, A. M. 2003. The South Caspian Basin: a review of its evolution from subsidence modelling. *Sedimentary Geology*, **156**, 119–148.

BUTLER, R. F. 1992. *Paleomagnetism: Magnetic Domains to Geologic Terranes*. Blackwell Scientific, Oxford.

CANDE, S. C. & KENT, D. V. 1995. Revised calibration of the geomagnetic polarity timescale for the Late Cretaceous and Cenozoic. *Journal of Geophysical Research*, **100**, 6093–6095.

CIUREJ, A. & HACZEWSKI, G. 2012. The Tylawa Limestones – a regional marker horizon in the Lower Oligocene of the Paratethys: diagnostic characteristics from the type area. *Geological Quarterly*, **56**, 833–844.

DA SILVA, A.-C., DEKKERS, M. J., MABILLE, C. & BOULVAIN, F. 2012. Magnetic susceptibility and its relationship with paleoenvironments, diagenesis and remagnetization: examples from the Devonian carbonates of Belgium. *Studies in Geophysics and Geodesy*, **56**, 677–704.

DEENEN, M., LANGEREIS, C., KRIJGSMAN, W., HACHIMI, H. E. & CHELLAI, E. H. 2011*a*. Palaeomagnetic results from Upper Triassic red-beds and CAMP lavas of the Argana Basin, Morocco. *In*: VAN HINSBERGEN, D. J. J., BUITER, S. J. H., TORSVIK, T. H., GAINA, C. & WEBB, S. J. (eds) *The Formation and Evolution of Africa: a Synopsis of 3.8 Ga of Earth History*. Geological Society, London, Special Publications, **357**, 195–209. https://doi.org/10.1144/SP357.10

DEENEN, M. H. L., LANGEREIS, C. G., VAN HINSBERGEN, D. J. J. & BIGGIN, A. J. 2011*b*. Geomagnetic secular variation and the statistics of palaeomagnetic directions. *Geophysical Journal International*, **186**, 509–520.

DILEK, Y., IMAMVERDIYEV, N. & ALTUNKAYNAK, Ş. 2010. Geochemistry and tectonics of Cenozoic volcanism in the Lesser Caucasus (Azerbaijan) and the peri-Arabian region: collision-induced mantle dynamics and its magmatic fingerprint. *International Geological Review*, **52**, 536–578.

EFENDIYEVA, M. A. 2004. Anoxia in waters of the Maikop paleobasin (Tethys Ocean, Azeri sector), with implications for the modern Caspian Sea. *Geo-Marine Letters*, **24**, 177–181.

ELLWOOD, B., CRICK, C., EL HASSANI, A., BENOIST, S. & YOUNG, R. 2000. Magnetosusceptibility event and cyclostratigraphy method applied to marine rocks: detrital input v. carbonate productivity. *Geology*, **28**, 1135–1138.

FORNACIARI, E., AGNINI, C., CATANZARITI, R., RIO, D., BOLLA, E. M. & VALVASONI, E. 2010. Mid-latitude calcareous nannofossil biostratigraphy, biochronology and evolution across the middle to late Eocene transition. *Stratigraphy*, **7**, 229–264.

GHORBANI, M. R. 2006. Lead enrichment in Neotethyan volcanic rocks from Iran: the implications of a descending slab. *Geochemistry Journal*, **40**, 557–568.

GOLONKA, J. 2004. Plate tectonic evolution of the southern margin of Eurasia in the Mesozoic and Cenozoic. *Tectonophysics*, **381**, 235–273.

GRADSTEIN, F. M., OGG, J. G. & SCHMITZ, M. 2012. *The Geologic Time Scale 2012*. Elsevier, Amsterdam.

GRIBBLE, R. F., STERN, R. J., NEWMAN, S., BLOOMER, S. H. & O'HEARN, T. 1998. Chemical and isotopic composition of lavas from the northern Mariana Trough: implications for magmagenesis in back-arc basins. *Journal of Petrology*, **39**, 125–154.

HACZEWSKI, G. 1996. Oligocene laminated limestones as a high-resolution correlator of palaeoseismicity, Polish Carpathians. *In*: KEMP, A. E. S. (ed.) *Palaeoclimatology and Palaeoceanography from Laminated Sediments*. Geological Society, London, Special Publications, **116**, 209–220. https://doi.org/10.1144/GSL.SP.1996.116.01.17

HANDLEY, H. K., MACPHERSON, C. G., DAVIDSON, J. P., BERLO, K. & LOWRY, D. 2007. Constraining fluid and sediment contributions to subduction-related magmatism in Indonesia: Ijen volcanic complex. *Journal of Petrology*, **48**, 1155–1183.

HAY, W. W. 1996. Tectonics and climate. *Geologische Rundschau*, **85**, 409–437.

HAY, W. W. 1998. Detrital sediment fluxes from continents to oceans. *Chemical Geology*, **145**, 287–323.

HUDSON, S. M., JOHNSON, C. L., EFENDIYEVA, M. A., ROWE, H. D., FEYZULLAYEV, A. A. & ALIYEV, C. S. 2008. Stratigraphy and geochemical characterization of the Oligocene–Miocene Maikop series: implications for the paleogeography of Eastern Azerbaijan. *Tectonophysics*, **451**, 40–55.

JOHNSON, C. L., HUDSON, S. M., ROWE, H. D. & EFENDIYEVA, M. A. 2010. Geochemical constraints on the Palaeocene-Miocene evolution of eastern Azerbaijan, with implications for the South Caspian basin and eastern Paratethys. *Basin Research*, **22**, 733–750.

JOVANE, L., COCCIONI, R., MARSILI, A. & ACTON, G. 2009. The late Eocene greenhouse-icehouse transition: observations from the Massignano global stratotype section and point (GSSP). *In*: KOEBERL, C. & MONTANARI, A. (eds) *The Late Eocene Earth–Hothouse, Icehouse, and Impacts*. Geological Society of America, Special Papers, **452**, 149–168.

KAZMIN, V. G., SBORTSHIKOV, I. M., ZONENSHAIN, L. P., BOULIN, J. & KNIPPER, A. L. 1986. Volcanic belts as markers of the Mesozoic-Cenozoic active margin of Eurasia. *Tectonophysics*, **123**, 123–152.

KIRSCHVINK, J. L. 1980. The least-squares line and plane and the analysis of palaeomagnetic data. *Geophysical Journal International*, **62**, 699–718.

KNIGHT, K. B., NOMADE, S., RENNE, P. R., MARZOLI, A., BERTRAND, H. & YOUBI, N. 2004. The Central Atlantic magmatic province at the Triassic–Jurassic boundary: paleomagnetic and ^{40}Ar/^{39}Ar evidence from Morocco for brief, episodic volcanism. *Earth and Planetary Science Letters*, **228**, 143–160.

KOPPERS, A. A. P. 2002. ArArCALC—software for ^{40}Ar/^{39}Ar age calculations. *Computers & Geosciences*, **28**, 605–619.

KUIPER, K. F., DEINO, A., HILGEN, F. J., KRIJGSMAN, W., RENNE, P. R. & WIJBRANS, J. R. 2008. Synchronizing rock clocks of Earth history. *Science*, **320**, 500–504.

LEE, J.-Y., MARTI, K., SEVERINGHAUS, J. P., KAWAMURA, K., YOO, H.-S., LEE, J. B. & KIM, J. S. 2006. A redetermination of the isotopic abundances of atmospheric Ar. *Geochimica Cosmochimica Acta*, **70**, 4507–4512.

LESS, G., ÖZCAN, E., PAPAZZONI, C. A. & STOCKAR, R. 2008. The middle to late Eocene evolution of

nummulitid foraminifer Heterostegina in the Western Tethys. *Acta Palaeontologica Polonica*, **53**, 317–350.

MARTINI, E. 1971. Standard Tertiary and Quaternary calcareous nannoplankton zonation. *In*: *Proceedings of the Second Planktonic Conference*. Tecnoscienza, Roma.

MCQUARRIE, N. & VAN HINSBERGEN, D. J. J. 2013. Retrodeforming the Arabia-Eurasia collision zone: age of collision v. magnitude of continental subduction. *Geology*, **41**, 315–318.

MIN, K., RENNE, P. R. & HUFF, W. D. 2001. $^{40}Ar/^{39}Ar$ dating of Ordovician K-bentonites in Laurentia and Baltoscandia. *Earth and Planetary Science Letters*, **185**, 121–134.

MORRISON, G. W. 1980. Characteristics and tectonic setting of the shoshonite rock association. *Lithos*, **13**, 97–108.

MOUTHEREAU, F., LACOMBE, O. & VERGÉS, J. 2012. Building the Zagros collisional orogen: timing, strain distribution and the dynamics of Arabia/Eurasia plate convergence. *Tectonophysics*, **532**, 27–60.

MULLENDER, T. A. T., VELZEN, A. J. & DEKKERS, M. J. 1993. Continuous drift correction and separate identification of ferrimagnetic and paramagnetic contributions in thermomagnetic runs. *Geophysical Journal International*, **114**, 663–672.

NALIVKIN, D. 1976. *Geological Map of Caucasus, Scale 1: 500,000*. Ministry of Geology, Moscow.

OKADA, H. & BUKRY, D. 1980. Supplementary modification and introduction of code numbers to the low-latitude coccolith biostratigraphic zonation (Bukry, 1973; 1975). *Marine Micropaleontology*, **5**, 321–325.

PASSIER, H. F., BOSCH, H. J. *ET AL.* 1999. Sulphidic Mediterranean surface waters during Pliocene sapropel formation. *Nature*, **397**, 146–149.

POPOV, S. V., RÖGL, F., ROZANOV, A. Y., STEININGER, F. F., SHCHERBA, I. G. & KOVAC, M. 2004. *Lithological-Paleogeographic Maps of Paratethys – 10-Maps Late Eocene to Pliocene*. Schweizerbart'sche Verlagsbuchhandlung, Stuttgart.

POPOV, S. V., SYCHEVSKAYA, E. K., AKHMET'EV, M. A., ZAPOROZHETS, N. I. & GOLOVINA, L. A. 2008. Stratigraphy of the Maikop Group and Pteropoda Beds in northern Azerbaijan. *Stratigraphy and Geological Correlation*, **16**, 664–677.

POUCLET, A., LEE, J.-S., VIDAL, P., COUSENS, B. & BELLON, H. 1994. Cretaceous to Cenozoic volcanism in South Korea and in the Sea of Japan: magmatic constraints on the opening of the back-arc basin. *In*: SMELLIE, J. L. (ed.) *Volcanism Associated with Extension at Consuming Plate Margins*. Geological Society, London, Special Publications, **81**, 169–191. https://doi.org/10.1144/GSL.SP.1994.081.01.10

RÖGL, F. 1998. Palaeogeographic considerations for Mediterranean and Paratethys seaways (Oligocene to Miocene). *Annales Naturhistorisches Museum Wien*, **99**, 279–310.

SACHSENHOFER, R. F., STUMMER, B., GEORGIEV, G., DELLMOUR, R., BECHTEL, A., GRATZER, R. & ĆORIĆ, S. 2009. Depositional environment and hydrocarbon source potential of the Oligocene Ruslar Formation (Kamchia Depression; Western Black Sea). *Marine and Petroleum Geology*, **26**, 57–84.

SAINT-GERMES, M. L., BAZHENOVA, O. K., BAUDIN, F., ZAPOROZHETS, N. I. & FADEEVA, N. P. 2000. Organic matter in Oligocene Maikop Sequence of the North Caucasus. *Lithology and Mineral Resources*, **35**, 47–62.

SCHULZ, H., BECHTEL, A., & SACHSENHOFER, R. F. 2005. The birth of the Paratethys during the early Oligocene: from Tethys to an ancient Black Sea analogue? *Global and Planetary Change*, **49**, 163–176.

SCHULZ, H.-M., SACHSENHOFER, R. F., BECHTEL, A., POLESNY, H. & WAGNER, L. 2002. The origin of hydrocarbon source rocks in the Austrian Molasse Basin (Eocene–Oligocene transition). *Marine and Petroleum Geology*, **19**, 683–709.

SERRA-KIEL, J., HOTTINGER, L. *ET AL.* 1998. Biostratigraphie des macroforaminifères du Paléocène et de l'Éocène de la Téthys. *Bulletin de la Société géologique de France*, **169**, 281–299.

SOTÁK, J. 2010. Paleoenvironmental changes across the Eocene-Oligocene boundary: insights from the Central-Carpathian Paleogene Basin. *Geologica Carpathica*, **61**, 393–418.

STEININGER, F. F. & WESSELY, G. 2000. From the Tethyan Ocean to the Paratethys Sea: Oligocene to Neogene stratigraphy, paleogeography and paleobiogeography of the circum-Mediterranean region and the Oligocene to Neogene Basin evolution in Austria. *Mitteilungen der Österreichischen Geologischen Gesellschaft*, **92**, 95–116.

SUN, S. S. & MCDONOUGH, W. F. 1989. Chemical and isotopic systematics of oceanic basalts: implications for mantle composition and processes. *In*: SAUNDERS, A. D. & NORRY, M. J. (eds) *Magmatism in the Ocean Basins*. Geological Society, London, Special Publications, **42**, 313–345.

TORABI, G. 2009. Subduction-related Eocene shoshonites from the Cenozoic Urumieh-Dokhtar magmatic arc (Qaleh-Khargooshi area, western Yazd Province, Iran). *Turkish Journal of Earth Sciences*, **18**, 583–613.

TYSON, R. V. & PEARSON, T. H. 1991. Modern and ancient continental shelf anoxia: an overview. *In*: TYSON, R. V. & PEARSON, T. H. (eds) *Modern and Ancient Continental Shelf Anoxia*. Geological Society, London, Special Publications, **58**, 1–24. https://doi.org/10.1144/GSL.SP.1991.058.01.01

VAN DER BOON, A. 2013. *Onset of Maikop sedimentation in the Talysh (Azerbaijan): climate or tectonics?* MSc thesis, Utrecht University, http://dspace.library.uu.nl/handle/1874/261949.

VAN VELZEN, A. J. & ZIJDERVELD, J. D. A. 1995. Effects of weathering on single-domain magnetite in Early Pliocene marine marls. *Geophysical Journal International*, **121**, 267–278.

VANDENBERGHE, N., HILGEN, F. J. *ET AL.* 2012. The Paleogene Period. *In*: GRADSTEIN, F. M., OGG, J. G., SCHMITZ, M. D. & OGG, G. M. (eds) *The Geologic Time Scale*. Elsevier, Boston, 855–921. https://doi.org/10.1016/B978-0-444-59425-9.00028-7

VERDEL, C., WERNICKE, B. P., HASSANZADEH, J. & GUEST, B. 2011. A Paleogene extensional arc flare-up in Iran. *Tectonics*, **30**, TC3008.

VETO, I. 1987. An Oligocene sink for organic carbon: upwelling in the Paratethys? *Palaeogeography, Palaeoclimatology, Palaeoecology*, **60**, 143–153.

Vincent, S. J., Allen, M. B., Ismail-Zadeh, A. D., Flecker, R., Foland, K. A. & Simmons, M. D. 2005. Insights from the Talysh of Azerbaijan into the Paleogene evolution of the South Caspian region. *Geological Society of America Bulletin*, **117**, 1513–1533.

Wade, B. S., Pearson, P. N., Berggren, W. A. & Pälike, H. 2011. Review and revision of Cenozoic tropical planktonic foraminiferal biostratigraphy and calibration to the geomagnetic polarity and astronomical time scale. *Earth-Science Reviews*, **104**, 111–142.

Yilmaz, A., Adamia, S., Chabukiani, A., Chkhotua, T., Erdoğan, K., Tuzcu, S. & Karabiyikoğlu, M. 2000. Structural correlation of the southern Transcaucasus (Georgia)-eastern Pontides (Turkey). *In:* Bozkurt, E., Winchester, J. A. & Piper, J. D. A. (eds) *Tectonics and Magmatism in Turkey and the Surrounding Area*. Geological Society, London, Special Publications, **173**, 171–182.

Zachos, J., Pagani, M., Sloan, L., Thomas, E. & Billups, K. 2001. Trends, global rhythms and aberrations in global climate 65 Ma to Present. *Science*, **292**, 686–693.

Zijderveld, J. D. A. 1967. AC demagnetization of rocks: analysis of results. *In*: Collinson, D. W. & Creer, K. M. (eds) *Methods in Paleomagnetism*. Elsevier, Amsterdam, 254–286.